RESEARCH ARTICLE

CARM1 Inhibition Enables Immunotherapy of Resistant Tumors by Dual Action on Tumor Cells and T Cells

Sushil Kumar[1,2], Zexian Zeng[3], Archis Bagati[1,2], Rong En Tay[1,2], Lionel A. Sanz[4], Stella R. Hartono[4], Yoshinaga Ito[1,2], Fieda Abderazzaq[5,6], Elodie Hatchi[5,6], Peng Jiang[3,7], Adam N.R. Cartwright[1,2], Olamide Olawoyin[1,8], Nathan D. Mathewson[1,2], Jason W. Pyrdol[1], Mamie Z. Li[9], John G. Doench[10], Matthew A. Booker[11], Michael Y. Tolstorukov[11], Stephen J. Elledge[9], Frédéric Chédin[4], X. Shirley Liu[3], and Kai W. Wucherpfennig[1,2,12]

ABSTRACT A number of cancer drugs activate innate immune pathways in tumor cells but unfortunately also compromise antitumor immune function. We discovered that inhibition of CARM1, an epigenetic enzyme and cotranscriptional activator, elicited beneficial antitumor activity in both cytotoxic T cells and tumor cells. In T cells, *Carm1* inactivation substantially enhanced their antitumor function and preserved memory-like populations required for sustained antitumor immunity. In tumor cells, *Carm1* inactivation induced a potent type 1 interferon response that sensitized resistant tumors to cytotoxic T cells. Substantially increased numbers of dendritic cells, CD8 T cells, and natural killer cells were present in *Carm1*-deficient tumors, and infiltrating CD8 T cells expressed low levels of exhaustion markers. Targeting of CARM1 with a small molecule elicited potent antitumor immunity and sensitized resistant tumors to checkpoint blockade. Targeting of this cotranscriptional regulator thus offers an opportunity to enhance immune function while simultaneously sensitizing resistant tumor cells to immune attack.

SIGNIFICANCE: Resistance to cancer immunotherapy remains a major challenge. Targeting of CARM1 enables immunotherapy of resistant tumors by enhancing T-cell functionality and preserving memory-like T-cell populations within tumors. CARM1 inhibition also sensitizes resistant tumor cells to immune attack by inducing a tumor cell–intrinsic type 1 interferon response.

INTRODUCTION

Many cancer drugs have been developed that induce apoptosis of tumor cells, for example by inducing DNA damage or inhibiting key signaling pathways required for cell proliferation (1). Although such drugs can induce substantial tumor shrinkage, recurrence is a major challenge due to outgrowth of drug-resistant tumor cells. The immune system could potentially target residual disease, but many of these tumor cell–targeted drugs also compromise immune cell survival/function or the production of immune cells by the hematopoietic system. For example, chemotherapy drugs kill not only dividing tumor cells but also rapidly dividing hematopoietic precursors and immune cells (2, 3).

Chemotherapy-induced DNA damage can induce activation of innate immune pathways in tumor cells, including the cGAS–STING pathway (4). The cGAS enzyme is activated by cytosolic double-stranded DNA, resulting in the synthesis of the cyclic dinucleotide cGAMP, which activates the STING receptor and thereby induces a powerful type 1 interferon response through the IRF3 transcription factor. Importantly, type 1 interferons also induce maturation of dendritic cells, a key step for T cell–mediated immunity (5). Some chemotherapy drugs are being used in combination with immunotherapy agents. For example, the combination of nab-paclitaxel and a PD-L1–blocking mAb was recently approved by the FDA for the treatment of metastatic triple-negative breast cancer (TNBC), but only a small fraction of treated patients benefited from this combination regimen compared with monotherapy with nab-paclitaxel (6). It is important to develop tumor cell–targeted drugs that enhance rather than compromise immune function.

The present study focuses on CARM1, an arginine methyltransferase that introduces asymmetric methylation of arginine residues in histone H3 and other chromatin-associated proteins. Asymmetric methylation refers to a highly specific modification in which two methyl groups are attached to one of the two nitrogen atoms of the arginine side chain (7). CARM1 acts as a transcriptional coactivator for nuclear hormone receptors and other transcription factors. It is recruited to chromatin by a member of the p160 family of proteins, which also recruits the p300/CBP histone acetyltransferases. Following recruitment, CARM1 enhances the activity of this coactivation complex by

[1]Department of Cancer Immunology and Virology, Dana-Farber Cancer Institute, Boston, Massachusetts. [2]Department of Immunology, Harvard Medical School, Boston, Massachusetts. [3]Department of Data Sciences, Dana-Farber Cancer Institute, Harvard T. H. Chan School of Public Health, Boston, Massachusetts. [4]Department of Molecular and Cellular Biology and Genome Center, University of California, Davis, California. [5]Department of Cancer Biology, Dana-Farber Cancer Institute, Boston, Massachusetts. [6]Harvard Medical School, Boston, Massachusetts. [7]Center for Cancer Research, National Cancer Institute, Bethesda, Maryland. [8]Yale School of Medicine, New Haven, Connecticut. [9]Department of Genetics, Harvard Medical School and Division of Genetics, Department of Medicine, Howard Hughes Medical Institute, Brigham and Women's Hospital, Boston, Massachusetts. [10]Broad Institute of Harvard and MIT, Cambridge, Massachusetts. [11]Department of Informatics and Analytics, Dana-Farber Cancer Institute, Boston, Massachusetts. [12]Department of Neurology, Brigham and Women's Hospital, Harvard Medical School, Boston, Massachusetts.

Note: Supplementary data for this article are available at Cancer Discovery Online (http://cancerdiscovery.aacrjournals.org/).

S. Kumar, Z. Zeng, A. Bagati, and R.E. Tay contributed equally to this study.

Corresponding Authors: Kai W. Wucherpfennig, Department of Cancer Immunology and Virology, Dana-Farber Cancer Institute, Smith Building, Room 736, 450 Brookline Avenue, Boston, MA 02215. Phone: 617-632-3086; E-mail: kai_wucherpfennig@dfci.harvard.edu; and Xiaole Shirley Liu, Department of Data Sciences, Dana-Farber Cancer Institute, Harvard T. H. Chan School of Public Health, Boston, MA 02215. Phone: 617-632-2472; E-mail: xsliu@ds.dfci.harvard.edu

methylation of arginine residues in p160, p300/CBP, and histone H3 (on residues H3R17 and H3R26; refs. 8–10). Overexpression of *CARM1* mRNA has been reported for many human cancer types, and in breast and prostate cancers it serves as a coactivator of transcription for estrogen α and androgen receptors (11, 12).

Using an *in vivo* CRISPR/Cas9 screen, we discovered that inactivation of the *Carm1* gene in T cells enhanced their antitumor function and increased the pool of tumor-infiltrating memory-like T cells, which are known to be required for sustained immunity. Recent work demonstrated that effector T-cell populations are maintained in tumors only when sufficient numbers of tumor-specific memory-like cells are present in the microenvironment (13, 14). Inactivation of *Carm1* in tumor cells elicited a potent T cell–dependent immune attack associated with greatly increased infiltration of tumors by CD8 T cells and dendritic cells. These data demonstrate that targeting of CARM1 induces potent tumor immunity by sensitizing resistant tumors to immune attack and enhancing antitumor T-cell function.

RESULTS

Discovery of *Carm1* as a Negative Regulator of Tumor-Infiltrating T Cells

We performed an *in vivo* CRISPR/Cas9 screen in tumor-specific T cells to discover negative regulators of antitumor immunity. A guide RNA (gRNA) library targeting epigenetic regulators was delivered into CD8 T cells using a lentiviral vector. These T cells originated from mice transgenic for Cas9 and the OT-I T-cell receptor (TCR), thus yielding a gene-edited library of T cells with defined antigen specificity (Fig. 1A). A total of 426 genes representing annotated epigenetic regulators were evaluated using three gRNA pools (5 gRNAs/gene plus 100 negative control gRNAs). Edited T cells were transferred to immunocompetent mice bearing subcutaneous B16F10 melanomas, which expressed the OVA antigen recognized by the OT-I TCR. Targeting of key negative regulators enhanced T-cell proliferation/survival within tumors and thus resulted in enrichment of the corresponding gRNAs. Representation of gRNAs was quantified after 10 days by deep sequencing of the gRNA cassette in T cells isolated from tumors or a control organ (spleen). gRNAs targeting the positive control genes *Pdcd1* and *Cblb* (encoding PD-1 and CBL-b proteins, respectively) were among the top enriched gRNAs in each of the three pools, demonstrating that key negative regulators could be reproducibly identified (Fig. 1B and C; Supplementary Table S1). The top hit from the primary screen was the *Carm1* gene, which encodes an arginine methyltransferase that introduces asymmetric dimethylation of histone H3 (H3R17 and H3R26 residues) and other nuclear proteins. This effect was specific for *Carm1* and not seen for genes encoding other arginine methyltransferases: although gRNAs targeting *Carm1* were enriched in tumor-infiltrating T cells relative to spleen, gRNAs targeting *Prmt1, Prmt2, Prmt5,* and *Prmt6* were depleted; also, no enrichment was observed for gRNAs targeting *Prmt3, Prmt7,* and *Prmt8*. We validated these results using a targeted gRNA library representing 31 top candidate genes, 2 positive control genes (*Pdcd1* and *Cblb*), and a set of control gRNAs. *Carm1* was again identified as the top hit in this validation screen (Supplementary Fig. S1A; Supplementary Table S1).

Carm1-knockout (KO) T cells were generated for functional experiments by electroporation of OT-I T cells with ribonucleoprotein complexes (RNP) composed of Cas9 protein and bound gRNAs. This transient editing procedure was effective, as shown by sequencing of genomic DNA and loss of CARM1 protein following editing with two different gRNAs (Supplementary Fig. S1B and S1C). A cytotoxicity assay demonstrated that *Carm1*-KO T cells were more effective in killing B16F10-OVA melanoma cells compared with control edited T cells (Fig. 1D; Supplementary Fig. S1D–S1F). Following coculture with B16F10-OVA tumor cells, *Carm1*-KO compared with control-KO T cells expressed higher levels of the CD69 activation marker, the granzyme B cytotoxicity protein, and the cytokines IL2, IFNγ, and TNFα (Supplementary Fig. S1G and S1H) and showed enhanced antigen-induced proliferation (Supplementary Fig. S1I). These data demonstrated that CARM1 was a negative regulator of tumor-specific T cells.

Carm1 Inhibition in CD8 T Cells Enhances Their Antitumor Function

Carm1-KO T cells were found to confer more effective antitumor immunity than control-KO CD8 T cells against B16F10-OVA tumors (Fig. 1E and F; Supplementary Fig. S2A). Flow cytometry analysis revealed greatly enhanced tumor infiltration by *Carm1*-KO compared with control-KO CD45.1+ CD8+ T cells, including increased accumulation of T cells that expressed the effector molecules granzyme B and IFNγ as well as the proliferation marker Ki-67 (Fig. 1G; Supplementary Fig. S2B). We confirmed enhanced antitumor immunity by *Carm1*-KO T cells using a second gRNA (Supplementary Fig. S2C and S2D).

Seven days following editing, OT-I CD8 T cells were cocultured for 24 hours with B16F10-OVA tumor cells. RNA-sequencing (RNA-seq) analysis demonstrated striking changes in gene expression, including upregulation of 1,143 genes and downregulation of 1,199 genes in *Carm1*-KO compared with control T cells (Fig. 2A and B; Supplementary Table S2). Upregulated genes encoded chemokine receptors that mediate T-cell recruitment into tumors (*Cxcr3*) and key genes required for maintenance of memory T-cell populations (transcription factors *Tcf7, Myb,* and *Bcl6;* surface receptors *Itgae* and *Cd27*). Downregulated genes included those associated with terminal differentiation (*Klrg1*), inhibition of cytokine signaling (*Socs1, Socs3*), and T-cell dysfunction within tumors (*Egr2*). To validate the RNA-seq results, we performed qPCR analysis using two different gRNAs and found that *Tcf7, Myb, Bcl6,* and *Itgae* (associated with T-cell memory) were upregulated in *Carm1*-KO compared with control-KO CD8 T cells, whereas *Klrg1* (associated with terminal differentiation) and *Havcr2* (associated with dysfunction) were downregulated in *Carm1*-KO T cells (Fig. 2C).

Gene set enrichment analysis (GSEA) highlighted "T-cell activation," "mitotic nuclear division," "Foxo signaling," and "regulation of leukocyte-mediated cytotoxicity" among the top pathways for genes overexpressed in *Carm1*-KO compared with control-KO T cells. Downregulated pathways related to RNA biology, protein translation, and DNA
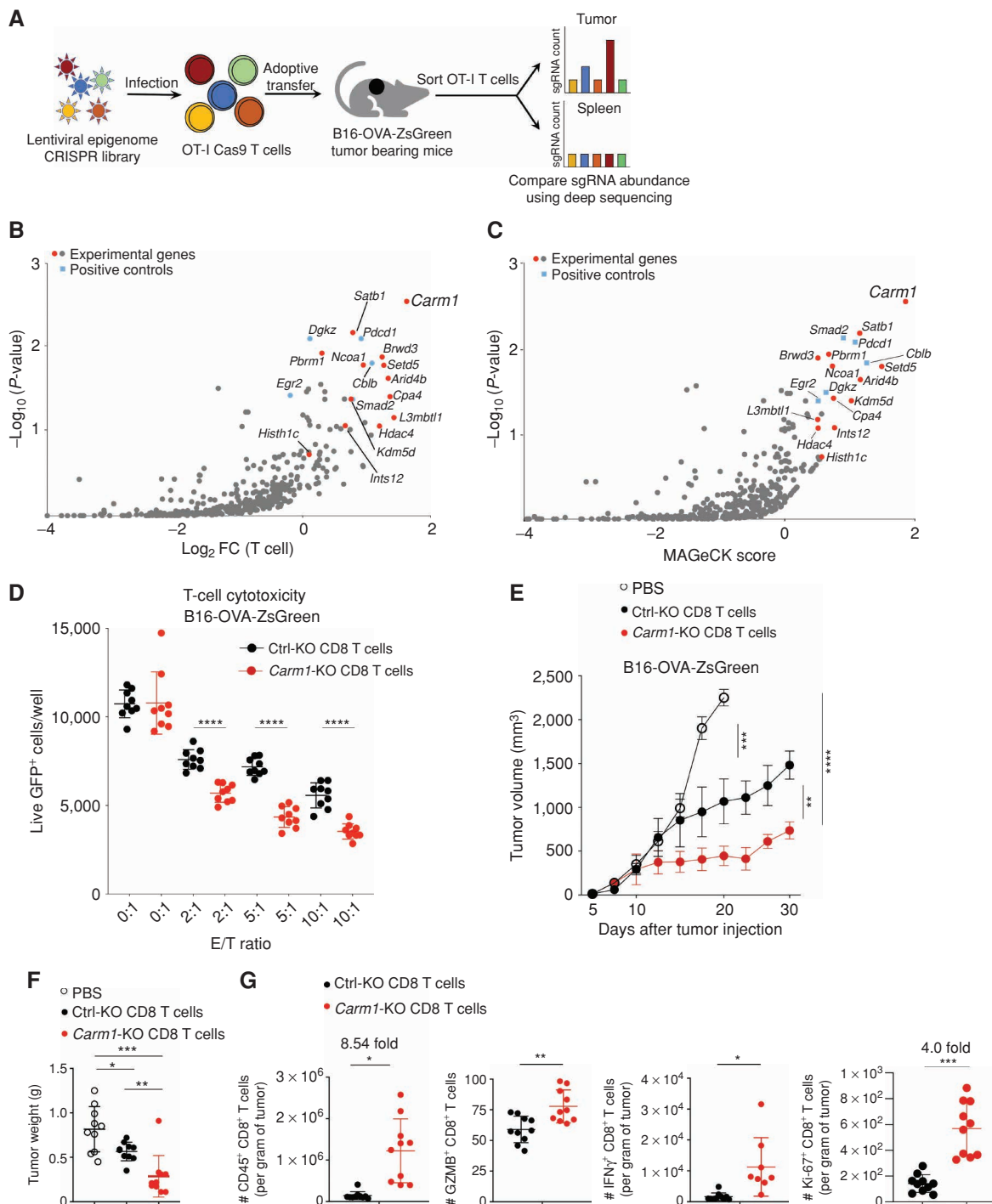
Figure 1. CARM1 is an epigenetic inhibitor in tumor-specific T cells. **A,** Experimental design for *in vivo* discovery of epigenetic regulators that inhibit CD8 T-cell accumulation in tumors. **B,** *In vivo* CRISPR screen with epigenetic gRNA library in tumor-specific CD8 T cells. gRNA quantification in CD8 T cells was compared in tumors (experimental site) and spleens (control organ; $\log_2$ fold change). Major experimental genes and positive control genes are highlighted in red and blue, respectively. **C,** MAGeCK analysis of *in vivo* CRISPR screen data; MAGeCK score provides integrated readout for strength of gene effects. **D,** T-cell cytotoxicity assay with *Carm1*-KO and control-KO OT-I CD8 T cells. CD8 T cells were edited by electroporation with Cas9 protein and bound gRNA, and cells were grown in IL15 + IL7 containing T-cell media for 5 days. T cells were cocultured with B16F10-OVA-ZsGreen tumor cells at indicated E/T ratios (*n* = 8–10/replicates per condition); 24 hours later, live GFP-positive tumor cells were counted using a Celigo image cytometer. Data are representative of three experiments and shown as mean ± SEM. ****, *P* < 0.0001, by unpaired two-sided Mann–Whitney test. **E,** Antitumor activity of adoptively transferred *Carm1*-KO or control-KO OT-I CD45.1 CD8 T cells. B16-OVA-ZsGreen tumor cells (0.1×10^6) were implanted subcutaneously. On day 7 after tumor cell inoculation, edited CD8 T cells (1×10^6) were transferred via tail-vein injection. Tumor size was recorded; *n* = 8–10 mice per group. **F,** Tumor weights 7 days following adoptive T-cell transfer for experiment shown in **E. G,** Flow cytometry analysis of tumor-infiltrating *Carm1*-KO or control-KO CD8 T cells following adoptive transfer of edited OT-I CD45.1 CD8 T cells (*n* = 10 mice/group) with gating on CD45.1 and CD8 T-cell markers. Quantification of CD8 T-cell infiltration and expression of effector (granzyme B, IFNγ) as well as proliferation (Ki-67) markers.
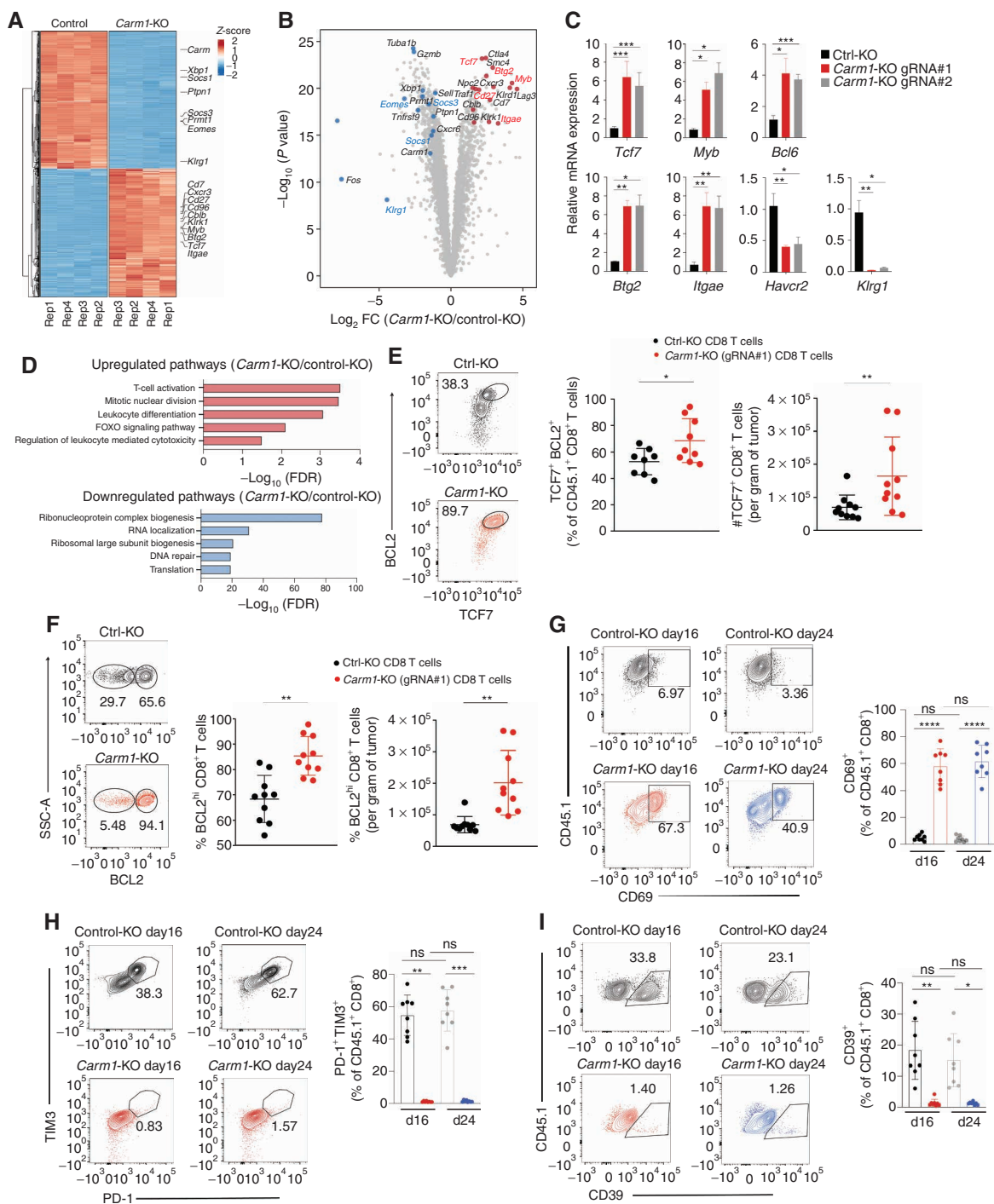
Figure 2. *Carm1*-KO in CD8 T cells enhances their antitumor function. **A,** RNA-seq analysis of differentially expressed genes in *Carm1*-KO or control-KO OT-I CD8 T cells cocultured for 24 hours with B16F10-OVA tumor cells (four biological replicates per condition). Color code represents *z* scores for differential gene expression. **B,** Volcano plot of all differentially expressed genes between *Carm1*-KO and control-KO OT-I CD8 T cells. Statistical significance (log$_{10}$ adjusted *P* value) was plotted against log$_2$ fold change of gene expression levels (*Carm1*-KO/control-KO cells). **C,** RT-qPCR analysis of *Tcf7, Myb, Bcl6, Btg2, Itgae, Havcr2,* and *Klrg1* mRNA levels in *Carm1*-KO and control-KO CD8 T cells (targeting of *Carm1* with two different gRNAs, triplicate measurements). **D,** Gene Ontology (GO) analysis of significantly upregulated/downregulated pathways in *Carm1*-KO versus control-KO T cells. **E,** Tumor-infiltrating *Carm1*-KO or control-KO CD8 T cells following adoptive transfer of edited OT-I CD45.1 CD8 T cells (*n* = 10 mice/group) with gating on CD45.1 and CD8 T-cell markers. Quantification of TCF7$^+$ T cells with high BCL2 protein levels and TCF7$^+$ CD8 T cells. **F,** Quantification of BCL-high tumor-infiltrating *Carm1*-KO or control-KO CD8 T cells. **G–I,** Tumor-infiltrating *Carm1*-KO or control-KO CD8 T cells were analyzed 16 or 24 days following adoptive transfer of edited OT-I CD45.1 CD8 T cells (*n* = 8 mice/group) with gating on CD45.1 and CD8 T-cell markers. Quantification of CD8 T activation marker (CD69; **G**) and markers of T-cell exhaustion (**H–I**). Data shown are representative of two experiments. Two-way ANOVA was used to determine statistical significance for time points when all mice were viable for tumor measurement. Graphs shown represent data summarized as mean ± SD and were analyzed by unpaired two-sided Mann–Whitney test. *, *P* < 0.05; **, *P* < 0.01; ***, *P* < 0.001; ****, *P* < 0.0001.

repair (Fig. 2D). Genes in the Foxo signaling pathway identified by GSEA included *Bcl6* and *Il7r*, both of which play important roles in T-cell memory. A large fraction of tumor-infiltrating *Carm1*-KO CD8 T cells were positive for TCF7 protein and also had high levels of BCL2, consistent with an increased pool of memory-like cells for *Carm1*-KO compared with control-KO T cells (Fig. 2E). Also, the number of tumor-infiltrating BCL2hi cells was substantially higher for *Carm1*-KO compared with control-KO CD8 T cells (Fig. 2F). We investigated T-cell persistence by studying tumor-infiltrating *Carm1*-KO and control-KO CD8 T cells at early (d16) and late (d24) time points following T-cell transfer. A significantly larger population of *Carm1*-KO CD8 T cells expressed the CD69 activation marker at both time points (Fig. 2G). Conversely, only a small percentage of *Carm1*-KO T cells coexpressed the PD-1 and TIM3 inhibitory receptors or CD39, which are markers of exhausted T cells (Fig. 2H and I). These data indicated that targeting of *Carm1* in CD8 T cells enhanced their antitumor function and maintained a substantial population of tumor-infiltrating T cells that expressed memory markers.

Inactivation of *Carm1* Gene in Tumor Cells Elicits Tumor Immunity

Analysis of RNA-seq data from 1,208 human cancer cell lines [Cancer Cell Line Encyclopedia (CCLE)] revealed high-level *CARM1* expression across a diverse range of human cancer cell lines (Fig. 3A). We therefore interrogated the role of CARM1 in tumor cells by inactivating the *Carm1* gene in murine cancer cell lines resistant to checkpoint blockade, including B16F10 melanoma and 4T1 breast cancer models (Fig. 3B and C). *In vitro* proliferation and survival of B16F10 and 4T1 cells were not affected by inactivation of the *Carm1* gene, but *in vivo* growth of *Carm1*-KO tumor cells was greatly diminished compared with control-KO tumor cells (Supplementary Fig. S2E; Fig. 3D; Supplementary Fig. S3A). Importantly, depletion of CD8 T cells restored the *in vivo* growth of *Carm1*-KO B16F10 cells, indicating that *Carm1* inactivation in tumor cells elicited potent T cell–mediated tumor immunity (Fig. 3D; Supplementary Fig. S3A). This conclusion was validated by comparing B16F10 tumor growth in immunocompetent wild-type and T cell–deficient T-cell receptor α (*Tcrα*) KO mice (Fig. 3E). Inactivation of the *Carm1* gene in the 4T1 model of TNBC and the MC38 colon cancer model also substantially slowed tumor growth and conferred a survival benefit (Fig. 3F–H). Importantly, the number of spontaneous pulmonary metastases was substantially reduced following orthotopic implantation of *Carm1*-KO compared with control-KO 4T1 tumor cells (Fig. 3G).

Next, we used an imaging-based T-cell cytotoxicity assay to examine whether inactivation of the *Carm1* gene sensitized tumor cells to killing by CD8 T cells. Indeed, *Carm1*-KO B16F10-OVA tumor cells were significantly more sensitive to T cell–mediated cytotoxicity than control-KO tumor cells, as shown by quantification of surviving live ZsGreen+ tumor cells or dying tumor cells labeled with a caspase 3/7 cell death reporter (Fig. 3I and J). A high-affinity small-molecule inhibitor of CARM1 was reported (EZM2302; ref. 15). Pretreatment of B16F10-OVA tumor cells with EZM2302 also

sensitized them to CD8 T cells (Fig. 3K). This CARM1 inhibitor also sensitized a human TNBC cell line to cytotoxic T cells. BT549 TNBC cells were cocultured with human CD8 T cells that expressed a TCR specific for a NY-ESO-1 peptide presented by HLA-A2:01. Pretreatment of these tumor cells with the CARM1 inhibitor (EZM2302) enhanced CD8 T cell–mediated cytotoxicity (Fig. 3L). These data demonstrated that inactivation of the *Carm1* gene in tumor cells induced potent T cell–mediated immunity and that *Carm1*-deficient tumor cells were more sensitive to T cell–mediated cytotoxicity.

Innate Immune Activation in *Carm1*-Deficient Tumor Cells

RNA-seq analysis demonstrated striking changes in the transcriptome of *Carm1*-KO versus control-KO B16F10 tumor cells. In particular, we observed increased expression of many interferon response genes in *Carm1*-KO compared with control-KO tumor cells, even though these tumor cells had not been exposed to exogenous type 1 interferon or IFNγ (Fig. 4A; Supplementary Fig. S3B; Supplementary Table S3). GSEA also highlighted transcriptional activation of the IFNα/γ and p53 pathways in *Carm1*-KO tumor cells (Fig. 4B; Supplementary Fig. S3C). In human melanoma, a higher type 1 interferon gene expression signature was found to correlate with increased CD8 T-cell infiltration (16). Importantly, there was little overlap in the genes that were differentially expressed as a consequence of *Carm1* gene inactivation in tumor cells compared with T cells (Fig. 4C). In particular, the p53 pathway and IFNα/γ response pathways were only transcriptionally activated in *Carm1*-KO tumor cells but not *Carm1*-KO T cells. Validation by RT-qPCR using two *Carm1* targeting gRNAs demonstrated that multiple interferon-stimulated genes (ISG), including *Irf7, Ccl5, Cxcl10, Ifit1, Oasl1*, and *Tap1*, were expressed at two- to sevenfold higher levels in *Carm1*-KO compared with control-KO tumor cells (Fig. 4D). Importantly, pretreatment of B16F10 cells with the CARM1 inhibitor EZM2302 also significantly increased the mRNA levels of these ISGs (Fig. 4E; Supplementary Fig. S3D). EZM2302 also induced the expression of a similar set of ISGs in human breast and melanoma cancer cell lines (Supplementary Fig. S3E and S3F).

The gene sets induced by type 1 interferons and IFNγ overlap substantially, and IFNγ secreted by activated T cells is an essential cytokine for protective tumor immunity (17). We therefore investigated whether inactivation of the *Carm1* gene in tumor cells enhanced their transcriptional response to IFNγ. Indeed, *Carm1*-KO B16F10 and 4T1 cells showed a heightened transcriptional response to IFNγ for all tested ISGs compared with control-KO tumor cells (Supplementary Fig. S3G and S3H). IFNγ stimulation also induced higher levels of STAT1 phosphorylation in *Carm1*-KO compared with control-KO B16F10 cells, even though total STAT1 and STAT2 protein levels were similar between the cell lines (Supplementary Fig. S4A). IFNγ inhibited the proliferation of *Carm1*-KO tumor cells more significantly than control-KO cells (Supplementary Fig. S4B). *Carm1*-KO tumor cells expressed moderately higher levels of MHC class I protein (H2-Kb) both in the absence of and following stimulation with IFNγ; PD-L1 levels were slightly higher for *Carm1*-KO
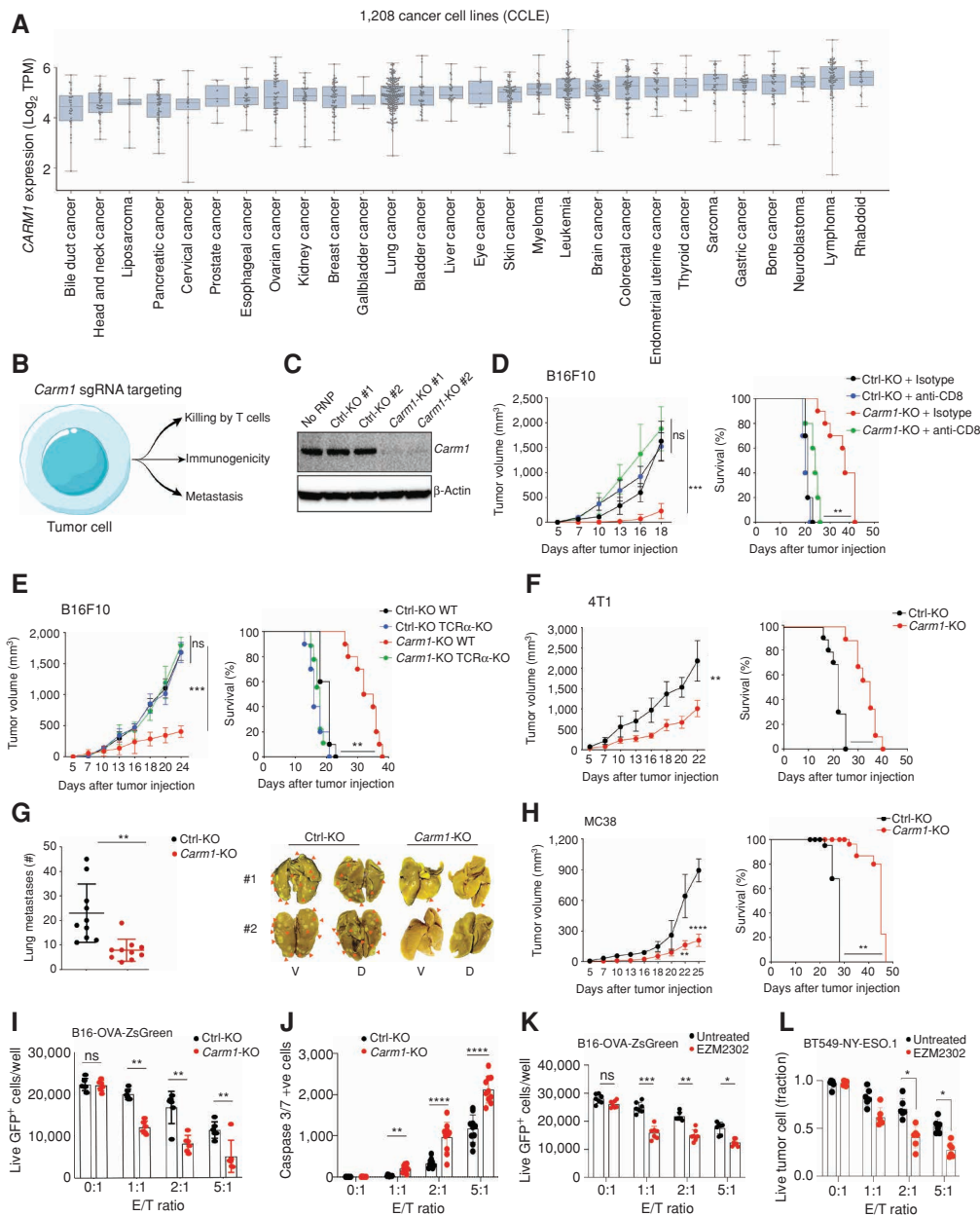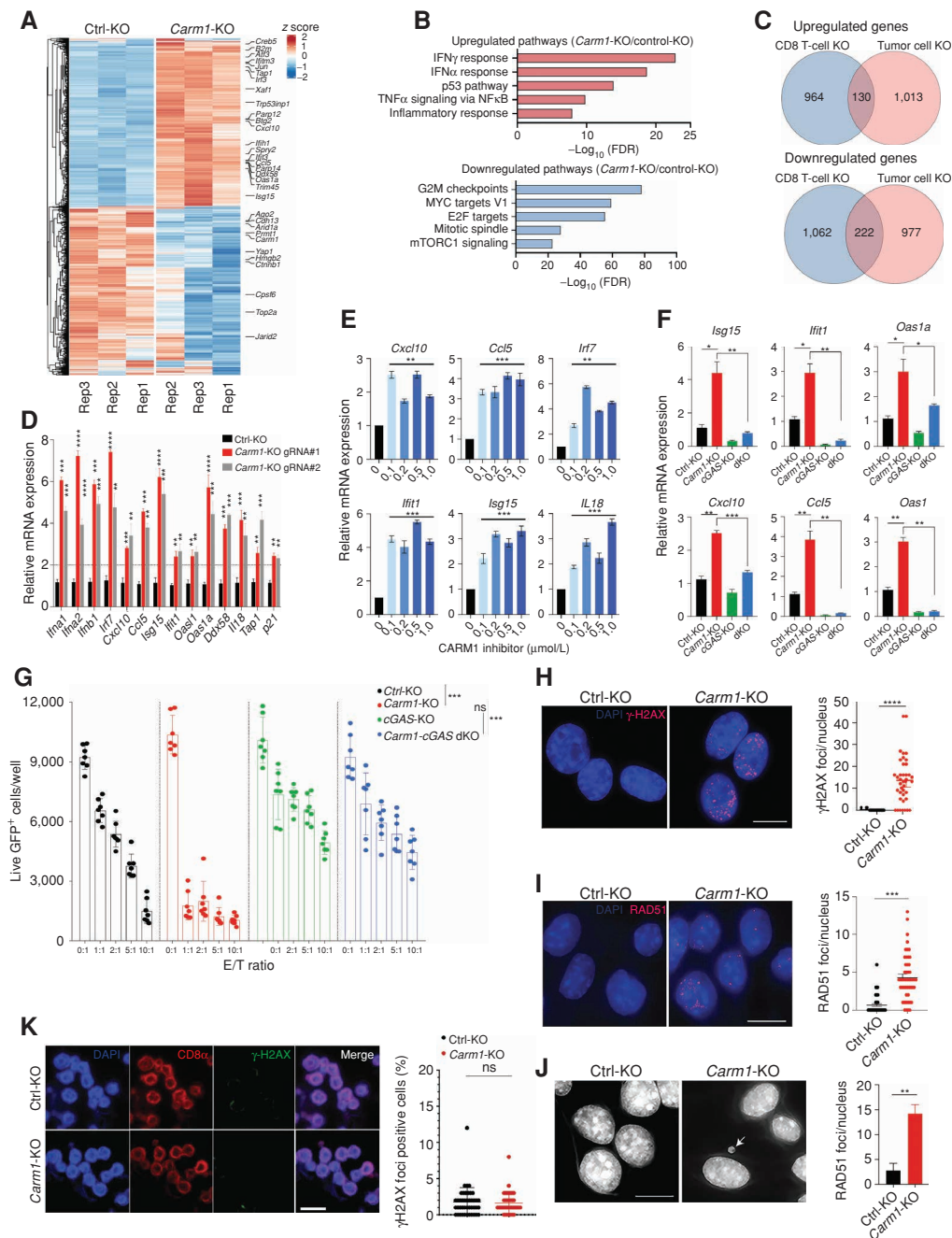
Figure 3. Inactivation of *Carm1* gene in tumor cells elicits tumor immunity. **A,** *CARM1* mRNA levels in a diverse panel of 1,208 cancer cell lines from the CCLE. Tumor cell lines were grouped based on cancer type. **B,** Strategy for targeting *Carm1* in tumor cells to study impact on T cell–mediated tumor immunity. **C,** Western blot analysis of CARM1 protein in B16F10 melanoma cells following electroporation with RNPs composed of Cas9 protein and bound gRNAs (control, *Carm1*); two different control and *Carm1* gRNAs were evaluated. **D,** Growth of *Carm1*-KO and control-KO B16F10 tumors (left) and survival of tumor bearing mice (right). Mice ($n = 8$–10/group) were treated with CD8 depleting or isotype control antibodies. This *in vivo* phenotype was confirmed with a second *Carm1* gRNA (Supplementary Fig. S3A). **E,** Growth of *Carm1*-KO tumors in T cell–deficient mice. *Carm1*-KO and control-KO B16F10 tumor cells (0.2×10^6) were implanted into immunocompetent or immunodeficient (*Tcra*-KO) mice ($n = 8$–10 mice/group); tumor growth (left) and survival (right) were recorded. **F,** Growth of *Carm1*-KO or control-KO 4T1 tumor cells following implantation into the mammary fat pad ($n = 8$–10 mice/group); tumor growth (left) and survival (right) were recorded. **G,** Quantification of spontaneous lung metastases formed by *Carm1*-KO or control-KO 4T1 tumors in immunocompetent mice. Representative images of lung metastases (V, ventral; D, dorsal; right). **H,** Tumor growth (left) and survival (right) following implantation of *Carm1*-KO and control-KO MC38 tumor cells ($n = 8$–10 mice/group). **I,** T-cell cytotoxicity assay with *Carm1*-KO or control-KO B16F10-OVA-ZsGreen tumor cells. Tumor cells were cocultured for 24 hours with OT-I CD8 T cells at indicated E/T ratios ($n = 8$–10 replicates per condition). **J,** Induction of tumor cell apoptosis (*Carm1*-KO or control-KO B16F10-OVA-ZsGreen cells) by CD8 T cells (as described in **I**), measured with a caspase 3/7 dye at different E/T ratios ($n = 8$–10 replicates/group). **K,** Sensitization of tumor cells to T cells with a CARM1 inhibitor. B16F10-OVA-ZsGreen tumor cells were pretreated with CARM1 inhibitor (EZM2302, 0.1 μmol/L) for 24 hours. Vehicle or inhibitor-treated tumor cells were cocultured with OT-I CD8 T cells at indicated E/T ratios ($n = 7$–8 replicates/condition). **L,** T-cell cytotoxicity assay with human BT549 TNBC and human CD8 T cells that expressed a NY-ESO-1 TCR. Tumor cells were pretreated with CARM1 inhibitor (EZM2302, 0.1 μmol/L) for 24 hours ($n = 7$–10 replicates/group); numbers of surviving tumor cells were quantified after 24 hours of coculture. Two-way ANOVA was used to determine statistical significance for tumor measurements at time points when all mice were alive. Statistical significance for survival of mice in each treatment group were calculated by log-rank (Mantel–Cox) test. Bar graphs represent data summarized as mean ± SEM and were analyzed by unpaired two-sided Mann–Whitney test. Data shown are representative of three experiments. *, $P < 0.05$; **, $P < 0.01$; ***, $P < 0.001$; ****, $P < 0.0001$; ns, nonsignificant.

Figure 4. Innate immune activation in *Carm1*-deficient tumor cells. **A,** RNA-seq analysis of differentially expressed genes in *Carm1*-KO and control-KO B16F10 tumor cells (*n* = 3/group). Data are representative of two independent experiments. **B,** Gene ontology (GO) analysis of significantly upregulated/downregulated genes in *Carm1*-KO compared with control-KO B16F10 tumor cells. **C,** Venn diagram representing number of overlapping differentially expressed genes in *Carm1*-KO tumor and CD8 T cells. **D,** Validation of ISGs by RT-qPCR in *Carm1*-KO compared with control-KO B16F10 cells (*n* = 3/group). **E,** RT-qPCR analysis of ISG mRNA levels following treatment of B16F10 cells with CARM1 inhibitor EZM2302 (0.1–1 μmol/L) or solvent control for 7 days (*n* = 3/group). **F,** Expression of selected ISGs in control-KO, *Carm1*-KO, *cGAS*-KO, and *Carm1/cGAS* double-KO (dKO) B16F10 cells analyzed by RT-qPCR (*n* = 3/group). **G,** T-cell cytotoxicity assay with control-KO, *Carm1*-KO, *cGAS*-KO, and *Carm1/cGAS* dKO B16F10 cells. Tumor cells were cocultured with OT-I CD8 T cells at indicated E/T ratios for 24 hours (*n* = 7–10 replicates/condition); live GFP-positive tumor cells were counted using a Celigo image cytometer. Data are shown as mean ± SEM. **H** and **I**, dsDNA damage in *Carm1*-KO versus control-KO B16F10 tumor cells based on labeling with γH2AX (**H**) and RAD51 (**I**) Abs. Representative immunofluorescence images (left) of γH2AX or RAD51 antibody labeling (red); nuclei labeled with DAPI. Quantification of number of γH2AX or RAD51 foci/nucleus (right). Data are shown as mean ± SEM. Scale bar, 10 μm. **J,** Detection of micronuclei in *Carm1*-KO and control-KO B16F10 tumor cells. DNA was labeled with DAPI; representative images (left) and quantification of cells positive for micronuclei (right). Data are shown as mean ± SEM. Scale bar, 10 μm. **K,** Analysis of *Carm1*-KO versus control-KO CD8+ T cells for dsDNA damage. OT-I CD8 T cells were plated 7 days post editing using CRIPSR/Cas9 as previously described and stained for CD8α, γH2AX, and DAPI. Representative immunofluorescence images of CD8α antibody labeling (red) and γH2AX antibody labeling (green); nuclei stained with DAPI (blue). Scale bar, 20 μm. Data shown in **D** to **J** are representative of three independent experiments. Bar graphs represent data summarized as mean ± SEM and were analyzed by unpaired two-sided Mann–Whitney test. *, P < 0.05; **, P < 0.01; ***, P < 0.001; ****, P < 0.0001; ns, nonsignificant. Error bars for all qPCR data represent SD with three replicates per group.

compared with control-KO tumor cells following IFNγ stimulation (Supplementary Fig. S4C and S4D). The enhanced transcriptional response of *Carm1*-KO tumor cells to IFNγ was attenuated when the *Ifnar1* gene was inactivated in *Carm1*-KO tumor cells, implicating enhanced type 1 interferon signaling in this process (Supplementary Fig. S4E). These data indicated that *Carm1*-KO tumor cells showed an increased responsiveness to IFNγ, an important cytokine secreted by activated T cells.

We next investigated which innate immune sensor was required for the interferon gene expression signature identified in *Carm1*-KO tumor cells. Inactivation of the *Mavs* gene, which encodes an essential adaptor protein for the double-stranded RNA sensors RIG-I and MDA-5, had no impact on expression of ISGs (Supplementary Fig. S5A and S5B). In striking contrast, inactivation of the *Cgas* gene greatly diminished mRNA levels of ISGs, indicating that the cGAS enzyme represented a key element in the innate immune pathway activated in *Carm1*-KO tumor cells (Fig. 4F; Supplementary Fig. S5C and S5D). We also tested whether activation of cGAS could explain the enhanced sensitivity of *Carm1*-KO tumor cells to cytotoxic T cells. Indeed, *Carm1*-KO tumor cells were highly sensitive to CD8 T cells, whereas inactivation of *Cgas* in *Carm1*-KO tumor cells rendered them substantially more resistant to cytotoxic T cells (Fig. 4G). Inactivation of *Cgas* (without inactivation of *Carm1*) also rendered B16F10-OVA tumor cells more resistant to T cells compared with wild-type B16F10-OVA cells. These data indicated that the enhanced sensitivity of *Carm1*-KO compared with control-KO tumor cells to cytotoxic T cells required a functional cGAS–STING pathway and that a lower level of activation of the cGAS–STING pathway in control-KO tumor cells was relevant for T cell–mediated killing.

These results strongly suggested that inactivation of *Carm1* induced a DNA damage response in tumor cells. DNA damage induces rapid phosphorylation of histone H2AX (γH2AX), which provides a sensitive readout for double-stranded DNA (dsDNA) breaks (18). Immunofluorescence analysis showed that a substantial fraction of *Carm1*-KO B16F10 cells had multiple nuclear foci labeled with a γH2AX antibody, whereas such foci were detected in only a small percentage of control-KO tumor cells (Fig. 4H). This conclusion was confirmed by labeling with an antibody specific for RAD51, another marker for dsDNA breaks (Fig. 4I). dsDNA breaks can induce chromosome missegregation during mitosis and formation of cytosolic micronuclei (19). Such micronuclei tend to have fragile nuclear envelopes, resulting in exposure of their dsDNA to cGAS (20). DAPI+ micronuclei were detected in a significantly larger percentage of *Carm1*-KO compared with control-KO tumor cells (Fig. 4J). A subset of these cytosolic DAPI+ micronuclei was positive for cGAS when an epitope-tagged version of cGAS was expressed in tumor cells (Supplementary Fig. S5E). CARM1 inhibitor treatment also induced γH2AX foci accumulation in B16F10 melanoma cells (Supplementary Fig. S5F). Using a gRNA targeting an intergenic region in the mouse genome, we confirmed that CRISPR/Cas9-based gene editing (>1 week prior to analysis) did not result in substantial dsDNA damage or ISG expression (Supplementary Fig. S5G and S5H). These results demonstrated that

inactivation of the *Carm1* gene induced innate immune activation within tumor cells caused by activation of the cGAS–STING pathway. CARM1 and p300 were previously shown to cooperate with BRCA1 and p53 to induce expression of the cell cycle inhibitor p21[CIP1] (CDKN1A; ref. 21). Failure of cell cycle inhibition following DNA damage can result in chromosome segregation during mitosis, formation of micronuclei, and cGAS activation (22).

Interestingly, unlike tumor cells, *Carm1* ablation did not induce dsDNA damage in CD8 T cells (Fig. 4K). Also, *Carm1* inactivation resulted in distinct gene expression changes in T cells versus tumor cells (Fig. 4C; Fig. 2A–C), suggesting that *Carm1* induced cell type–specific consequences in T cells (enhanced function, preserved pool of memory-like cells) compared with tumor cells (DNA damage and induction of cGAS–STING signaling).

CARM1 Inhibition Overcomes Resistance to Checkpoint Blockade

Many human tumor types resistant to checkpoint blockade with CTLA4 or PD-1 mAbs are poorly infiltrated by CD8 T cells ("cold tumors"). Poor infiltration by CD8 T cells is associated with an absence of a type 1 interferon gene expression signature (23, 24). We hypothesized that treatment with a CARM1 inhibitor could be effective in checkpoint blockade–resistant tumors by enhancing the function of tumor-specific T cells and also increasing the sensitivity of tumor cells to cytotoxic T cells. B16F10 melanomas are resistant to monotherapy with CTLA4 or PD-1 mAbs and even combination therapy with both checkpoint antibodies (25). Treatment of *Carm1*-KO tumors with CTLA4 or PD-1 blockade substantially reduced tumor growth and conferred a significant survival benefit (Fig. 5A; Supplementary Fig. S6A). Importantly, small molecule–mediated CARM1 inhibition (EZM2302) also sensitized B16F10 melanomas to checkpoint blockade with a CTLA4 mAb and resulted in a significant survival benefit (Fig. 5B). The inhibitor was administered at a dose of 150 mg/kg, but optimization of drug dose for this application was not feasible due to limited availability of this compound. This inhibitor was previously evaluated only in an immunodeficient mouse model and shown to moderately slow the *in vivo* growth of a human multiple myeloma cell line (RPMI-8226; ref. 15). The highly metastatic 4T1 model of TNBC is also resistant to CTLA4 blockade. Inactivation of the *Carm1* gene sensitized 4T1 tumors to CTLA4 blockade and conferred a marked survival benefit compared with the three other experimental groups (Fig. 5C). CTLA4 mAb-treated mice with *Carm1*-KO 4T1 tumors also showed a substantial reduction in the number of spontaneous lung metastases, again in comparison to all other treatment groups (Fig. 5D).

Analysis of *Carm1*-KO B16F10 tumors showed a striking increase in the number of infiltrating CD8 T cells and a substantial reduction in the percentage of CD8 T cells that expressed the inhibitory PD-1 and TIM3 inhibitory receptors (Fig. 5E–G). In contrast, the number of tumor-infiltrating CD4 T cells (calculated per gram of tumor) was similar between all treatment groups, although the percentage of CD4 T cells in the total T-cell pool was lower in *Carm1*-KO compared to control-KO tumors due to the striking increase in CD8 T-cell accumulation (Supplementary Fig. S6B; Fig. 5E).
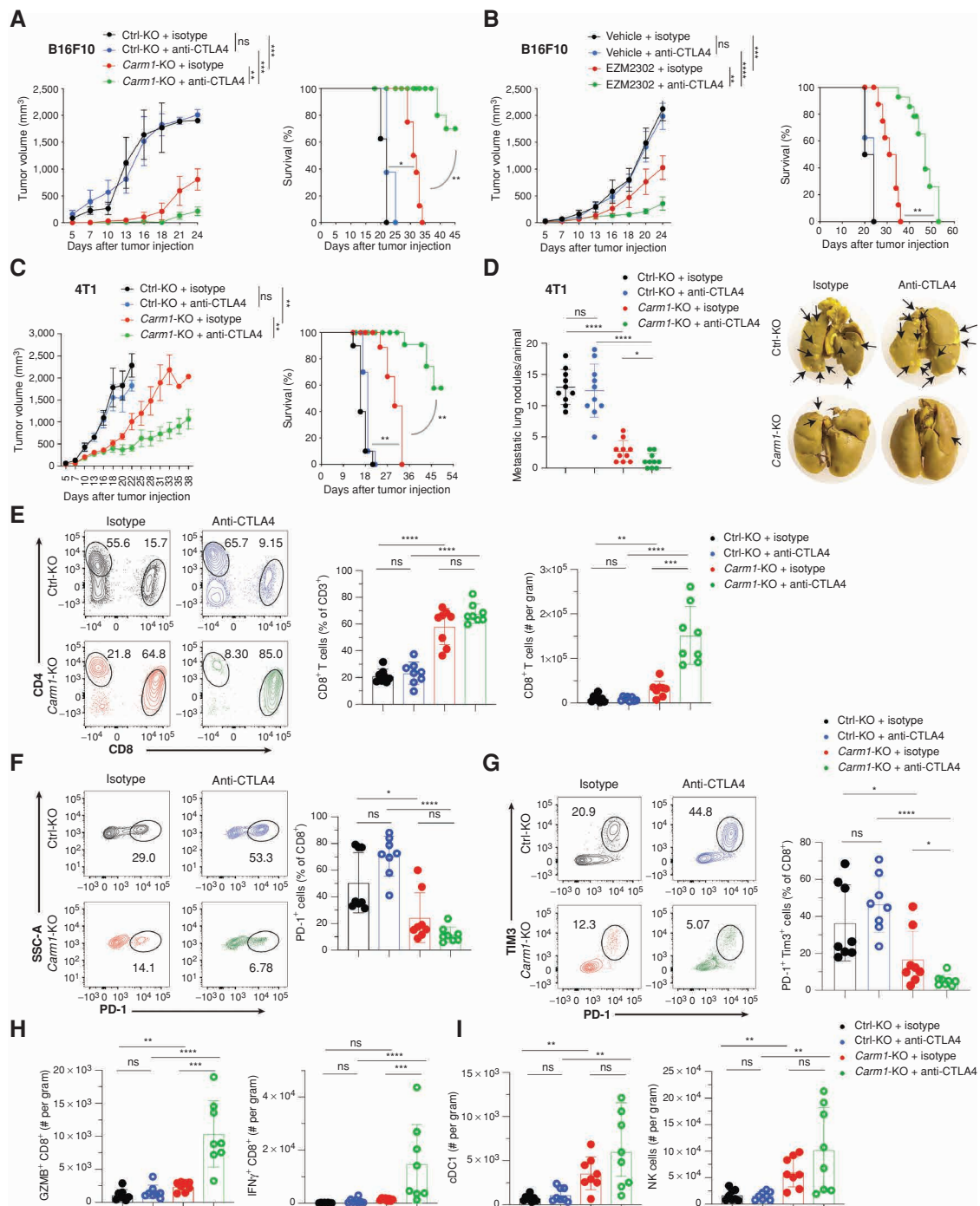
Figure 5. CARM1 inhibition overcomes resistance to checkpoint blockade. **A,** Treatment of *Carm1*-KO or control-KO B16F10 tumors with CTLA4 or isotype control antibodies ($n = 8$ mice/group). Tumor growth (left) and survival of tumor-bearing mice (right) are shown. Mice bearing comparable tumor volume (~50 mm^3) were randomized into different treatment groups. **B,** Treatment of B16F10 tumors with CARM1 inhibitor (EZM2302) or vehicle control in combination with CTLA4 or isotype control antibodies ($n = 8$ mice/group). EZM2302 (150 mg/kg twice a day) was orally administered for 2 weeks (days 7–21). **C,** Treatment of *Carm1*-KO or control-KO 4T1 tumors with anti-CTLA4 or isotype control antibodies ($n = 8$ mice/group). **D,** Change in number of spontaneous lung metastases (left) and representative images of lung metastases formed by 4T1 tumors treated as described in **C** (right; $n = 8$ mice/group). **E,** Quantification of tumor-infiltrating CD8 T cells in *Carm1*-KO and control-KO B16F10 tumors ($n = 8$ mice/group) following treatment with CTLA4 or isotype control antibodies (day 18 after tumor cell implantation). Representative flow plots (left) and quantification of CD8 T cells as percentage of CD3$^+$ cells and per gram of tumor (middle and right, respectively). **F** and **G,** Quantification of PD-1–positive and PD-1/TIM3 double-positive tumor-infiltrating CD8$^+$ T cells for experiment described in **E**. **H** and **I,** Quantification of CD8 T cells expressing effector markers (GZMB and IFNγ), migratory cross-presenting cDC1 (CD45$^+$/CD3$^-$/F4/80-/CD11c$^+$/MHC-II^{high}/CD103$^+$/CD11b$^-$), and NK cells (CD45$^+$/CD3$^-$/CD49b$^+$) per gram of tumor for the experiment described in **E**. Data shown are representative of two experiments. Two-way ANOVA was used to determine statistical significance for time points when all mice were viable for tumor measurement. Log-rank (Mantel–Cox) test was used to determine statistical significance for survival of mice. Bar graphs represent data summarized as mean ± SEM and were analyzed by unpaired two-sided Mann–Whitney test. *, $P < 0.05$; **, $P < 0.01$; ***, $P < 0.001$; ****, $P < 0.0001$; ns, nonsignificant.

CTLA4 mAb treatment further enhanced CD8 T-cell infiltration into *Carm1*-KO B16F10 tumors compared with the three other experimental groups and reduced the percentage of CD8 T cells double positive for the PD-1 and TIM3 inhibitory receptors (Fig. 5E–G). Also, a substantially larger percentage of CD8 T cells from *Carm1*-KO compared with control-KO CTLA4-treated tumors were positive for key functional markers, including granzyme B and IFNγ (Fig. 5H; Supplementary Fig. S6C). *Carm1*-KO tumors (treated with control or CTLA4 mAbs) were also infiltrated by a larger number of dendritic cells, including cross-presenting dendritic cells (cDC1), as well as natural killer (NK) cells, compared with control-KO tumors treated with either mAb (Fig. 5I; Supplementary Fig. S6D). Similar changes were observed in *Carm1*-KO 4T1 tumors in particular following treatment with a CTLA4 mAb (Supplementary Fig. S6E–S6I). These data demonstrated that tumor cell–intrinsic inactivation of the *Carm1* gene induced multiple significant changes in the tumor microenvironment, including enhanced infiltration by CD8 T cells, NK cells, and dendritic cells. Also, CD8 T cells expressed substantially lower levels of the PD-1 and TIM3 inhibitory receptors, consistent with a reduced level of T-cell exhaustion.

We also investigated the impact of CARM1 inhibitor treatment on the tumor immune microenvironment, both as monotherapy as well as in combination with PD-1 or CTLA4 mAbs (Supplementary Figs. S7–S9). In toxicity studies with this CARM1 inhibitor, we did not observe any histologic changes in a comprehensive analysis of major organs or weight loss between the CARM1 inhibitor versus solvent control treatment groups (Supplementary Fig. S7A and S7B). CD8 T-cell infiltration was substantially increased following monotherapy with the CARM1 inhibitor and was even higher when the inhibitor was combined with PD-1 or CTLA4 mAbs (Supplementary Fig. S8A). In contrast, CD8 T-cell infiltration was not increased following PD-1 or CTLA4 monotherapy compared with the isotype control antibody group. We also observed a striking increase in the number of CD8 T cells (per gram of tumor) that expressed granzyme B, IL2, IFNγ, and perforin in all three CARM1 inhibitor treatment groups (Supplementary Fig. S8B–S8E). In contrast, PD-1 expression by CD8 T cells was reduced in CARM1 inhibitor treatment groups compared with the vehicle control group (Supplementary Fig. S8F). CARM1 inhibitor treatment did not change the number of tumor-infiltrating CD4 T cells or FOXP3+ regulatory T cells (Tregs). However, the CD8/FOXP3 Treg ratio was substantially increased in all three CARM1 treatment groups because of the increase in CD8 T-cell infiltration (Supplementary Fig. S9A–S9D). Interestingly, tumor-infiltrating NK cells were also increased in all three CARM1 inhibitor treatment groups and were highest when the CARM1 inhibitor was combined with PD-1 or CTLA4 mAbs. cDC1 were increased when the CARM1 inhibitor was combined with PD-1 or CTLA4 mAbs, but no changes in macrophage numbers were detected across any of the treatment groups (Supplementary Fig. S9E). These data demonstrated that small molecule–mediated inhibition of CARM1 induced major favorable changes in the tumor immune microenvironment, in particular for CD8 T cells, NK cells, and cDC1. These favorable changes were further enhanced when the CARM1 inhibitor was combined with PD-1 or CTLA4 mAbs.

To examine whether reexpression of *Carm1* in tumor cells reversed the phenotype induced by *Carm1* inactivation, we introduced a *Carm1* cDNA under the control of a doxycycline (Dox)-inducible promoter into *Carm1*-KO B16F10 tumor cells (Supplementary Fig. S10A and S10B). Dox treatment suppressed mRNA levels of IFNγ-inducible genes in *Carm1*-KO cells, consistent with our finding that control-KO tumor cells showed lower responsiveness to IFNγ than *Carm1*-KO tumor cells (Supplementary Figs. S10C and S3G–S3H). Control-KO B16F10 tumor cells transduced with the empty vector showed rapid growth, regardless of whether mice were treated with vehicle or Dox (Supplementary Fig. S10D). As expected, *Carm1*-KO tumor cells transduced with the *Carm1* vector but treated with vehicle grew slowly, with similar kinetics as *Carm1*-KO tumor cells transduced with the empty vector. In contrast, Dox treatment substantially accelerated growth of *Carm1*-KO tumor cells transduced with the *Carm1* vector. Importantly, key aspects of the tumor microenvironment were also reversed by Dox-induced reexpression of *Carm1* in *Carm1*-KO tumor cells, including the striking degree of CD8 T-cell infiltration, lower levels of PD-1 expression by CD8 T cells, and the increase in cDC1 infiltration (Supplementary Fig. S11A–S11D).

TDRD3 and MED12 Are Effector Molecules of the CARM1 Pathway

CARM1 deposits H3R17me2a and H3R26me2a methyl-arginine marks on histone tails that are recognized by the Tudor domain–containing protein TDRD3 (26). CARM1 also methylates a number of other nuclear proteins, including MED12, a component of the regulatory arm of the Mediator complex (27). We found that inactivation of either *Tdrd3* or *Med12* genes in B16F10 cells increased mRNA levels of multiple ISGs, similar to inactivation of *Carm1* (Fig. 6A and B; Supplementary Fig. S12A–S12D). Furthermore, this ISG gene expression signature was lost when the *Cgas* gene was also inactivated in *Tdrd3*-KO or *Med12*-KO B16F10 cells (Fig. 6A and B). Similar to *Carm1* ablation, *Tdrd3* or *Med12* inactivation resulted in higher sensitivity to IFNγ and led to enhanced IFNγ-induced expression of ISGs (Supplementary Fig. S12E and S12F). Inactivation of genes encoding other TDRD3- or MED12-associated proteins (*Top3b, Top1,* and *Med13*) did not result in a substantial increase in ISG mRNA levels except for some upregulation of ISGs in *Med13*-KO tumor cells (Supplementary Fig. S12G–S12I). Inactivation of *Tdrd3* or *Med12* genes in B16F10 tumor cells also resulted in accumulation of γH2AX-positive nuclear foci and cytosolic micronuclei, as described above for *Carm1*-KO B16F10 cells (Fig. 6C and D). Finally, we found that *Tdrd3*-KO tumors showed substantially attenuated growth and that this phenotype was again CD8 T cell–dependent (Fig. 6E and F). CTLA4 mAb treatment further inhibited the growth of *Tdrd3*-KO tumor cells and resulted in survival of a large fraction of the mice (Fig. 6G).

Biochemical studies showed that MED12 was indeed a direct target of CARM1. When MED12 was immunoprecipitated from control-KO B16F10 cells, asymmetric methylation of arginine residues of MED12 could be readily detected by
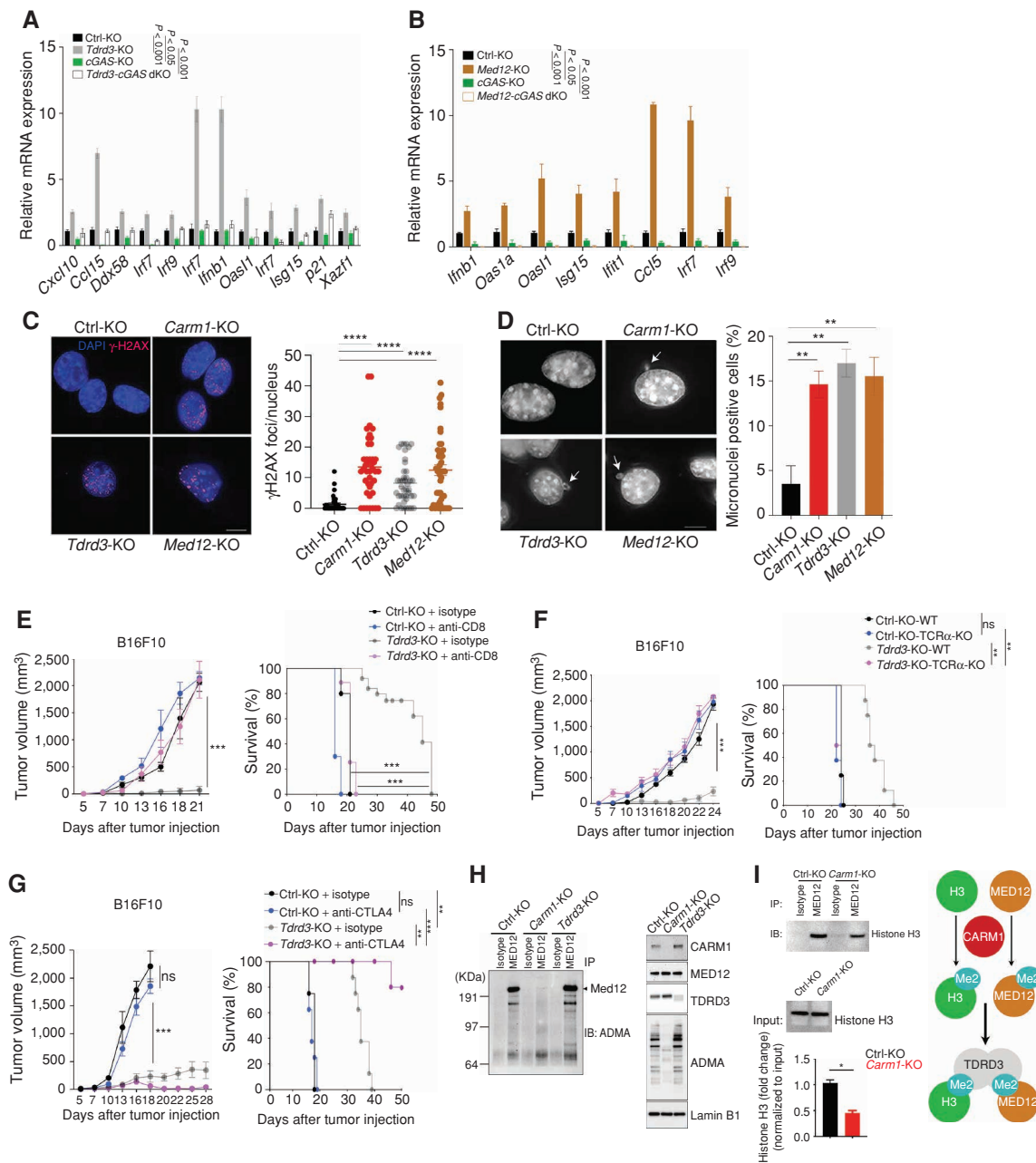
Figure 6. TDRD3 and MED12 are downstream effectors of CARM1. **A,** Comparison of ISG expression in control-KO, *Tdrd3*-KO, *cGAS*-KO, and *Tdrd3-cGAS* dKO B16F10 cells by RT-qPCR (*n* = 3/group). **B,** Comparison of ISG expression in control-KO, *Med12*-KO, *cGAS*-KO, and *Med12-cGAS* dKO B16F10 cells by RT-qPCR (*n* = 3/group). **C,** Immunofluorescence analysis of dsDNA damage by γH2AX antibody staining (red foci; nuclei labeled with DAPI) in control-KO, *Carm1*-KO, *Tdrd3*-KO, and *Med12*-KO B16F10 tumor cells (left). Images for control-KO and *Carm1*-KO reshown from Fig. 4 to illustrate comparison to other KO tumor cell lines. Quantification of number of γH2AX foci/nucleus for each cell line (right). Scale bar, 10 μm. **D,** Analysis of micronuclei in control-KO, *Carm1*-KO, *Tdrd3*-KO, and *Med12*-KO B16F10 tumor cells using DAPI as a DNA stain. Representative images (left) and quantification of percentage of cells with micronuclei (right). Scale bar, 10 μm. **E,** Tumor growth and survival of mice bearing control-KO and *Tdrd3*-KO B16F10 tumors. Mice were treated with CD8 T cell–depleting or isotype control antibodies (*n* = 8–10 mice/group). **F,** Tumor growth and survival of control-KO and *Tdrd3*-KO B16F10 tumors in immunocompetent and T cell–deficient (*Tcra*-KO) mice (*n* = 8–10 mice/group). **G,** Tumor growth and survival of anti-CTLA4 or isotype control antibody treated mice bearing *Tdrd3*-KO or control-KO B16F10 tumors (*n* = 8 mice/group). **H,** Arginine methylation of *Med12* by CARM1. Immunoprecipitation of MED12 protein from nuclear extracts of control-KO, *Carm1*-KO, or *Tdrd3*-KO B16F10 tumor cells, followed by Western blot detection with an antibody specific for asymmetric dimethylation of arginine residues (ADMA; left). Western blot analysis of nuclear extracts from the same cell lines with antibodies for the indicated proteins (right). **I,** Effect of *Carm1* on interaction of MED12 with histone H3. Immunoprecipitation of MED12 protein from control-KO or *Carm1*-KO B16F10 tumor cells, followed by Western blot detection with histone H3 antibody (top). Input levels of histone H3 in immunoprecipitated samples are shown (middle); quantification of histone H3 bound to MED12 normalized to total histone H3 (bottom). Graph shows proposed biochemical interactions (right). Two-way ANOVA was used to determine statistical significance for time points when all mice were viable for tumor measurement. Statistical significance for survival of mice in each treatment group was calculated by log-rank (Mantel–Cox) test. Bar graphs represent data summarized as mean ± SEM and were analyzed by unpaired two-sided Mann–Whitney test. Data are representative of three (**A–H**) and two (**I**) experiments. *, $P < 0.05$; **, $P < 0.01$; ***, $P < 0.001$; ****, $P < 0.0001$; ns, nonsignificant.

Western blot analysis (Fig. 6H), consistent with a previous report that identified MED12 as a target of CARM1 (27). This asymmetric methylation of arginine residues of MED12 was absent in *Carm1*-KO B16F10 tumor cells (but not in *Tdrd3*-KO tumor cells, as expected). Furthermore, immunoprecipitation of MED12 from nuclear lysates showed that less histone H3 was bound to MED12 in *Carm1*-KO compared with control-KO cells, indicating that CARM1 facilitated recruitment of MED12 to histone H3 (Fig. 6I). These results demonstrated that inactivation of the *Tdrd3* and *Med12* genes resulted in a similar immune-mediated phenotype as inactivation of the *Carm1* gene.

We further investigated whether RNA Pol II–mediated transcription was altered in *Carm1*-KO compared with control-KO tumor cells. Western blot analysis of the C-terminal domain (CTD) of RNA Pol II showed increased phosphorylation of Ser2 (pSer2, a mark of transcriptional elongation; ref. 28) and Ser5 in nuclear lysates from *Carm1*-KO compared with control-KO cells (Supplementary Fig. S13A). We systematically investigated Pol II phosphorylation using mammalian native elongating transcript sequencing (mNET-seq; ref. 29). Inactivation of the *Carm1* gene increased the normalized read density of pSer2 CTD Pol II tags relative to total Pol II tags around immediate promoter regions of genes (Supplementary Fig. S13B and S13C). Also, ~25% of the genes upregulated in *Carm1*-KO compared with control-KO cells were associated with higher normalized RNA Pol II pSer2 status (Supplementary Fig. S13D). GSEA of these overlap genes showed an enrichment in the p53 pathway, consistent with the data presented in Fig. 4 (Supplementary Fig. S13E). These data provided evidence for altered transcriptional regulation in *Carm1*-deficient tumor cells, consistent with the identification of MED12 as a CARM1 target. Furthermore, increased abundance of alternatively spliced genes (exon gains in 638 genes and exon losses in 708 genes) was found in *Carm1*-KO tumor cells. Pathway analysis using these alternatively spliced genes identified DNA repair, regulation of transcription, and chromatin organization to be among top enriched pathways in *Carm1*-KO tumor cells (Supplementary Fig. S13F). Cotranscriptional R-loop structures have been linked to genome instability and are thought to be resolved through TDRD3 and TOP3B (30). We used S9.6-based DNA/RNA immunoprecipitation sequencing approaches (DRIP-seq; ref. 31) to determine whether R-loops were increased as a result of *Carm1*-KO. No significant trend toward R-loop gains was observed (Supplementary Fig. S13G), arguing that cotranscriptional R-loops over genic regions were not a source of the genomic instability observed in *Carm1*-KO cells.

Relevance of CARM1 in Human Cancers

We next investigated the relevance of CARM1 in human cancers, including a potential role of CARM1 in tumor cells. We found that gene signatures for a number of important pathways were downregulated in human cancer cell lines with high versus low *CARM1* mRNA levels, including the p53, MHC class I antigen presentation, and interferon-related pathways (Fig. 7A; Supplementary Table S4). These results suggested that CARM1 also served an important role in human tumor cells by inhibiting important immune pathways.

Analysis of RNA-seq data sets from The Cancer Genome Atlas (TCGA) indicated that CARM1 may regulate immune responses in human cancers. In a large number of human cancer types, *CARM1* mRNA levels were negatively correlated with gene signatures of tumor infiltration by T cells and antigen-presenting cells (APC) as well as response to IFNγ and IFNα (Fig. 7B; Supplementary Fig. S14A). Furthermore, *CARM1* mRNA levels positively correlated with a gene signature for tumor infiltration by immunosuppressive myeloid-derived suppressor cells. To better understand the effect of *CARM1* expression in human tumors, we performed an analysis of differentially regulated pathways for two of the cancer types investigated above (TCGA skin cutaneous melanoma and lung squamous cell carcinoma). Tumors with high versus low *CARM1* mRNA levels showed downregulation of IFNγ and IFNα response pathways, whereas pathways related to MYC target V1/V2 and G2M checkpoints were upregulated (Fig. 7C).

RNA-seq data from TCGA enable analysis of a large number of tumors but lack single-cell resolution. We therefore also investigated the malignant cell populations in independent human tumor single-cell RNA-seq (scRNA-seq) data sets from multiple cancer types. Again, we found that high *CARM1* mRNA levels negatively correlated with p53 and DNA repair pathways as well as key immune pathways (APC infiltration and response to IFNα/IFNγ); high *CARM1* mRNA levels were also associated with reduced survival in a number of human cancer types (Fig. 7D; Supplementary Figs. S14B, S14C, S15A, and S15B).

We also examined *CARM1* gene expression in clinical immune checkpoint blockade (ICB) data sets, analyzing 16 clinical trial data sets. Low expression of *CARM1* per se was not associated with ICB response. Given that MED12 was a downstream target of CARM1, we investigated the role of *MED12* and *CARM1* mRNA levels on response to PD-1 pathway inhibition: we first separated the cohorts based on *MED12* mRNA levels and then examined the correlation of *CARM1* mRNA levels in *MED12* low (<median) and *MED12* high (>median) cohorts. In four clinical cohorts, we found that ICB responders had significantly lower expression levels of both *MED12* and *CARM1* compared with nonresponders (two trials of PD-1 blockade in melanoma, one trial of PD-L1 blockade in kidney cancer, one trial of PD-1 blockade in glioblastoma; ref. Fig. 7E). In addition, higher levels of a *Carm1*-KO gene expression signature were associated with response to ICB in four clinical cohorts; this signature was obtained from RNA-seq analysis of *Carm1*-KO versus control-KO B16F10 tumor cells (Supplementary Fig. S16A; Supplementary Table S5). In TCGA RNA-seq data sets, this *Carm1*-KO signature positively correlated with gene signatures of CD8 T-cell infiltration, antigen processing and presentation, as well as IFNγ response (Supplementary Fig. S16B). These data provided evidence that CARM1 expression was associated with major immune pathways in human cancers.

DISCUSSION

In this study, we report a novel immunotherapy approach for tumors resistant to checkpoint blockade. Many human
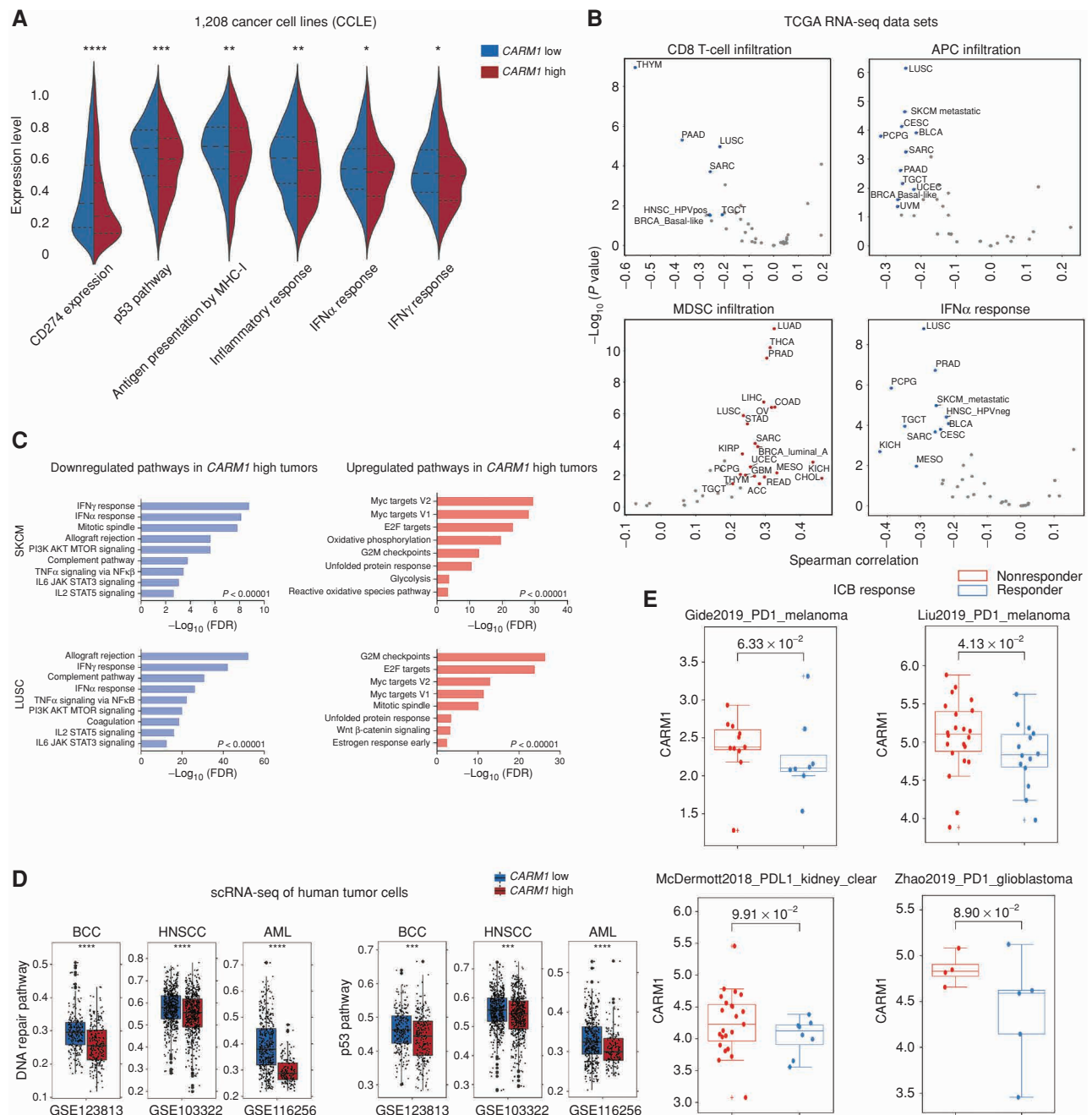
Figure 7. Relevance of *CARM1* in human cancers. **A,** Analysis of indicated pathways across a diverse panel of 1,208 human cancer cell lines (CCLE). Symmetric violin plots illustrate stratifications for *CARM1* high and low cell lines using median expression levels. **B,** Analysis of TCGA RNA-seq data across human cancer types. Correlation of *CARM1* mRNA levels with indicated pathways. Plots show Spearman correlation and estimated statistical significance for indicated pathways in different cancer types adjusted for tumor purity. Each dot represents a cancer type in TCGA. **C,** Gene ontology (GO) analysis of significantly upregulated/downregulated genes in *CARM1* high tumor cells in skin cutaneous melanoma (SKCM; n = 442 patients) and lung squamous cell carcinoma (LUSC; n = 363 patients) data sets (TCGA PanCancer Atlas). **D,** Analysis of scRNA-seq data of malignant cells from three human cancer cohorts [GSE123813: basal cell carcinoma (BCC); GSE103322: head and neck cancer squamous cell carcinoma (HNSCC); GSE116256: acute myeloid leukemia (AML)]. Scores for DNA repair and p53 pathways are shown. Data were stratified by *CARM1* high and low groups using median expression levels. Statistical comparisons were made using two-sided unpaired Mann–Whitney tests. **E,** Correlation of *CARM1* mRNA levels with response to ICB in patients with cancer treated with PD-1 or PD-L1 mAbs. The analysis is shown for tumors with low (<median) *MED12* mRNA levels. *CARM1* mRNA levels did not correlate with response to ICB in tumors with high (>median) *MED12* mRNA levels. The P values were inferred by Mann–Whitney U test.

cancers fail to respond to PD-1 and/or CTLA4 antibodies, and these resistant tumors frequently lack significant infiltration by CD8 T cells ("cold" tumors; ref. 32). In essence, such tumors are not sufficiently immunogenic to elicit a spontaneous T-cell response that can be enhanced by checkpoint blockade. Priming of a tumor-specific cytotoxic T-cell response requires recruitment of cDC1 into tumors, followed by activation and migration of dendritic cells into tumor-draining lymph nodes, where they prime naive CD8 T cells (33). These cellular events require activation of innate immune signals that induce production of key chemokines and cytokines, including type 1 interferons that activate dendritic cells. We show here that this barrier to effective cancer immunotherapy can be overcome by inhibition of CARM1, an epigenetic regulator. Interestingly, CARM1 inhibition in either tumor cells or T cells had major beneficial effects on T cell–mediated tumor immunity. Inactivation of CARM1 in tumor cells induced a type 1 interferon response and resulted in substantially increased numbers of tumor-infiltrating CD8 T cells, NK cells, and dendritic cells. Also, these tumor-infiltrating CD8 T cells showed higher functionality and lower expression of exhaustion markers. Inactivation of CARM1 in T cells preserved a substantial pool of tumor-infiltrating memory-like CD8 T cells with enhanced antitumor function. These findings are significant because T-cell exhaustion and loss of tumor-infiltrating memory populations are considered to represent major barriers to protective tumor immunity. We provide substantial evidence that this pathway is relevant in human cancers. Analysis of TCGA data demonstrated high *CARM1* mRNA levels across a wide range of human cancer types, including human cancers that have thus far been largely resistant to checkpoint blockade. *CARM1* mRNA levels were negatively correlated with gene expression signatures of key immune pathways, including the MHC class I antigen presentation, type 1 interferon, and IFNγ pathways. These human data are consistent with previous publications which demonstrated that a type 1 gene expression signature is associated with T cell–inflamed ("hot") as opposed to non–T cell–inflamed ("cold") tumors (32).

Why does inhibition of CARM1 elicit such distinct responses in T cells versus tumor cells? Inactivation of *Carm1* in T cells greatly increased CD8 T-cell accumulation in tumors. RNA-seq analysis of *Carm1*-KO compared with control-KO T cells indicated that *Carm1* inactivation reduced terminal effector differentiation (reduced expression of *Klrg1*), which is known to impair T cell–mediated tumor immunity. Rather, *Carm1*-KO T cells expressed higher levels of transcription factors critical for differentiation, self-renewal, and persistence of memory T cells, including *Tcf7* and *Myb* (34). A recent scRNA-seq analysis of CD8 T cells in human melanomas demonstrated that higher expression of *TCF7* by CD8 T cells predicted a positive outcome in patients treated with checkpoint blockade (35). *Carm1*-KO T cells expressed higher levels of *Myb*, which encodes a transcription factor that promotes memory T-cell formation by transcriptional activation of *Tcf7* and repression of *Zeb2*. *Myb* overexpression was previously shown to enhance CD8 T-cell memory formation and polyfunctionality, as well as promote protective antitumor immunity (36). These data are

consistent with the hypothesis that CARM1 acts as a cotranscriptional activator that promotes terminal differentiation of tumor-infiltrating T cells.

In contrast, inactivation of *Carm1, Tdrd3*, and *Med12* in tumor cells resulted in induction of a type 1 interferon response that sensitized tumors to T cell–mediated attack. This type 1 interferon response was accompanied by DNA damage, formation of micronuclei, and cGAS–STING activation. These findings are consistent with the previous finding that CARM1 cooperates with BRCA1 and p53 to induce expression of the cell cycle inhibitor p21[CIP1] (CDKN1A; ref. 21). Cell cycle progression despite the presence of double-stranded DNA breaks can result in chromosome missegregation during mitosis and the formation of micronuclei that activate the cGAS–STING pathway (37). Interestingly, no DNA damage was observed in T cells, even though these cells can undergo rapid proliferation following triggering of the T-cell receptor. We considered the possibility that the DNA damage phenotype in tumor cells was caused by accumulation of genic R-loops, but DRIP-seq did not demonstrate increased formation of R-loops in *Carm1*-KO compared with control-KO tumor cells. Many genes involved in the DNA damage response represent tumor suppressors and are inactivated in tumor cells because of mutations or epigenetic mechanisms. We hypothesize that CARM1 inactivation in tumor cells amplifies preexisting DNA damage by interfering with p53-induced inhibition of cell cycle progression. This hypothesis could explain why CARM1 inhibition induces cGAS–STING activation in tumor cells but not T cells.

Some chemotherapy drugs can induce activation of the cGAS–STING pathway in tumor cells, but targeting of the cell cycle is detrimental to hematopoietic precursors and proliferating tumor-specific T cells. Also, a number of small-molecule STING agonists have been developed that are delivered by intratumoral injection (38). The approach presented here may be particularly relevant in the setting of metastatic disease resistant to checkpoint blockade by sensitizing tumor cells to T cells and improving persistence of cytotoxic T cells. Inactivation of the *Carm1* gene in tumor cells combined with CTLA4 blockade induced a substantial survival benefit in B16F10 melanoma and 4T1 TNBC models. Importantly, a small-molecule inhibitor of CARM1 also showed synergy with a CTLA4 blocking mAb in the B16F10 melanoma model that is resistant even to the combination of PD-1 and CTLA4 mAbs. This inhibitor greatly increased tumor infiltration by CD8 T cells, NK cells, and cross-presenting dendritic cells. These data provide the rationale for targeting of CARM1 in human cancers resistant to current immunotherapies. This approach may be useful for not only checkpoint blockade therapy, as illustrated here, but also other immunotherapy approaches in which T cells serve as key effector cells, including neoantigen-based cancer vaccines and chimeric antigen receptor (CAR) T-cell therapies for solid-tumor indications. In adoptive T-cell therapies, CARM1 inhibition may not only sensitize resistant solid tumors to cytotoxic T cells but also enhance T-cell memory and persistence, which are critical for sustained clinical benefit with such cellular therapies (39).

METHODS

Cell Lines

B16F10, 4T1, and MC38 parental cell lines were purchased from ATCC. B16-OVA-ZsGreen cells were generated by lentiviral transduction of the parental line with a pHAGE expression vector driving expression of an N-terminally truncated variant of chicken ovalbumin (subcloned from pcDNA3-deltaOVA, Addgene plasmid #6459525). zsGreen+ cells were sorted to purity to establish the cell line. B16-OVA-zsGreen cells were validated for expression of zsGreen and cell surface presentation of the OVA peptide SIINFEKL in complex with H2-K[b]. Furthermore, the cells were tested for their ability to activate OT-I CD8 T cells. Murine *Carm1* cDNA was synthesized and cloned into pINDUCER21-ORF-EG (Addgene plasmid #46948) using gBlocks from IDT to generate the Dox–*Carm1* construct. Empty vector or Dox–*Carm1*–transduced B16F10 control-KO or *Carm1*-KO cells were sorted for purity based on GFP expression. Dox-inducible CARM1 protein expression was confirmed by Western blotting. B16F10 and 4T1 cells were grown in DMEM and RPMI media, respectively, supplemented with 10% FBS and 1% penicillin/streptomycin. MC38 cells were grown in DMEM supplemented with 10% FBS, 100 IU/mL penicillin/streptomycin, 5 mmol/L nonessential amino acids, 5 mmol/L sodium pyruvate, and 5 mmol/L HEPES at 37°C with 5% CO$_2$. Cell lines were validated for *Mycoplasma* contamination using the ATCC Universal Mycoplasma Detection Kit.

Mice

Six- to 8-week-old male mice were used for all experiments. WT C57BL/6 mice (JAX stock #000664), BALB/c (JAX stock #000651), and *Tcrα*-KO mice (JAX stock #002116) were purchased from the Jackson Laboratory. OT-I mice (JAX stock #003831) were crossed with the CD45.1 congenic strain (JAX stock #002014). OT-I Cas9 double-transgenic mice were generated by crossing OT-I mice (JAX stock #003831) with mice carrying a Rosa26-targeted knock-in of *Streptococcus pyogenes* Cas9 (JAX stock #024858) with constitutive Cas9 expression. The presence of the Cas9 transgene was verified according to genotyping protocols published by Jackson Laboratory. All purchased mice were acclimated for 1 week to housing conditions at the Dana-Farber Cancer Institute Animal Resource Facility prior to all experiments. Colonies for each strain of mice were maintained in the same animal facility. Mice were housed in pathogen-free conditions and in accordance with the animal care guidelines from the Dana-Farber Cancer Institute (DFCI) standing committee on animals and the NIH. Animal protocols were approved by the DFCI Institutional Animal Care and Use Committee.

In Vivo *CRISPR/Cas9 Screen in Tumor-Infiltrating CD8 T Cells*

Cloning of Epigenetic gRNA Library and Virus Production. For the primary screen, we constructed three lentiviral plasmid libraries of gRNA sequences targeting a total of 426 genes that encoded epigenetic regulators. Each library contained five unique gRNA sequences that targeted 142 candidate genes. In addition, gRNAs targeting six genes previously shown to inhibit CD8 T-cell accumulation in tumors were included as positive controls (*Pdcd1, Ctla4, Cblb, Egr2, Smad2*, and *Ppp2r2d*). We also included 100 gRNA sequences as negative controls. These gRNA libraries were cloned into the lentiviral plasmid vector pLKO–gRNA–Thy1.1 that drove expression of the Thy1.1 surface marker. For this purpose, the pLKO.3G vector (Addgene plasmid #14748) was modified by replacing eGFP with the Thy1.1 coding sequence. gRNA libraries were then cloned into the resulting lentiviral expression vector.

For the validation screen, a new gRNA library was constructed by targeting 31 genes selected from the top hits of the primary screens as well as *Pdcd1* and *Cblb* as positive control genes (six gRNAs/gene; Genetic Perturbation Platform, Broad Institute). As negative controls, 186 gRNAs were added (93 nontargeting plus 93 intergenic gRNAs).

To generate lentivirus for transduction with pooled gRNA libraries, the following transfection mix was generated for each 162-cm^2 tissue culture flask of HEK293T cells: 7 µg pLKO–gRNA–Thy1.1 plasmid prep containing lentiviral gRNA sequence libraries, 7 µg pCMV–DR.9.1, and 0.7 µg pCMV-VSV-G in 700 µL OPTI-MEM serum-free media (Gibco) plus 42 µL TransiT-293 transfection reagent (Mirus). This transfection mix was added to low-passage HEK293T cells (80%–90% confluence) in 162-cm^2 tissue culture flasks followed by overnight incubation. The next day, the media were removed and replaced with 20 mL RPMI supplemented with 20% FCS. Viral supernatants were collected at 48 and 72 hours posttransduction (2 × 20 mL supernatant total per 162-cm^2 flask), passed through a 0.45-µmol/L filtration unit (ThermoFisher) and concentrated by ultracentrifugation at 112,000 × *g*. Viral titers were determined by transducing HEK293T cells with serial dilutions of a small aliquot of the concentrated prep and measuring the percentage of Thy1.1-positive HEK cells by flow cytometry.

Transduction of OT-I Cas9 CD8 T Cells. Spleens and peripheral lymph nodes (inguinal, axillary, and cervical nodes) from OT-I Cas9 mice were mechanically dissociated using 70-µmol/L cell strainers in complete RPMI medium [containing 10% FBS + 1× GlutaMax (Gibco), 100 U/mL penicillin-streptomycin, 1 mmol/L sodium pyruvate, 20 mmol/L HEPES, and 50 µmol/L 2-mercaptoethanol]. OT-I Cas9 CD8 T cells (≥97% purity) were isolated from single-cell suspensions using an EasySep Mouse CD8+ T Cell Isolation Kit (Stemcell Technologies) according to the manufacturer's instructions. T cells were cultured in complete RPMI media supplemented with 100 ng/mL IL15 (Biolegend) and 5 ng/mL IL7 (Biolegend) for 48 hours. T cells were then transduced with lentiviral gRNA libraries by spin infection with concentrated lentivirus preps [multiplicity of infection (MOI) = 15] using retronectin-coated (Takara Bio) 24-well non–tissue culture–treated plates (2 × 10^6 cells/well). Spin infection was done at 2,000 rpm for 1.5 to 2 hours at 32°C in a total volume of 1 mL virus prep plus complete RPMI media supplemented with 5 µg/mL protamine sulphate (Sigma-Aldrich). Cells were cultured for 72 hours posttransduction in complete RPMI media supplemented with 50 ng/mL IL15 and 2.5 ng/mL IL7 (Biolegend) before magnetic enrichment of Thy1.1+ cells using an EasySep Mouse CD90.1 Positive Selection Kit (StemCell Technologies); this approach resulted in purity of Thy1.1+ cells of ≥93%.

***In Vivo *Screen with Tumor-Infiltrating CD8 T Cells.* gRNA-transduced Thy1.1+ OT-I Cas9 CD8 T cells (5 × 10^6) were injected intravenously into each of 10 to 12 C57BL/6 mice with B16-OVA-ZsGreen tumors (≥25 mm^2 tumor area). On day 10 following T-cell transfer, tumors and spleens were isolated for recovery of transferred Thy1.1+ CD8 T cells. Tumors were dissociated using GentleMACS C tubes (Miltenyi Biotec) on a GentleMACS dissociator (Miltenyi Biotec) with the "37C_m_TDK_1" program and an enzyme mix containing 1 mg/mL collagenase D (Sigma-Aldrich), 20 U/mL DNase I (Sigma Aldrich), and 100 µg/mL hyaluronidase type V (Sigma-Aldrich) in RPMI media (without additional supplements). Total tumor cell suspensions were then centrifuged at 50 × *g* for 5 minutes, and supernatants were collected. Spleens were mechanically dissociated using 70-µmol/L cell strainers, and total CD8 T cells were then isolated using EasySep Mouse CD8+ T Cell Isolation Kits (Stemcell Technologies) according to the manufacturer's instructions. Live singlet Thy1.1+ TCRβ+ CD8+ CD4− cells were sorted from tumor and spleen suspensions using a FACSAria IIIu cell sorter (BD)

equipped with a 70-μmol/L nozzle and the "Yield" purity mask to ensure complete collection of events. Cell pellets were washed once with cold PBS, and genomic DNA was extracted with a Zymogen Quick-gDNA Microprep Kit following the manufacturer's protocol for suspension cells.

Sequencing of gRNA Libraries and Quantification of gRNA Representation. Genomic DNA isolated from tumor-infiltrating OT-I Thy1.1+ CD8 T cells was subjected to PCR amplification of the gRNA cassette for Illumina sequencing of gRNA representation by the Genetic Perturbation Platform of the Broad Institute of MIT and Harvard (Cambridge, MA). Protocols for PCR amplification and Illumina sequencing are described in detail at https://portals.broad-institute.org/gpp/public/resources/protocols.

Data analysis was performed using Model-based Analysis of Genome-wide CRISPR-Cas9 Knockout (MaGeCK; ref. 40). For candidate gene discovery, the normalized gRNA count table was loaded into MaGeCK by comparing tumor (experimental) and spleen (control) conditions described above. Top genes were determined based on mean $\log_2$ fold change (LFC) for all gRNAs and false discovery rate (FDR).

Assays with Edited T Cells and Tumor Cells

Editing of Genes in Tumor Cells. Cells were edited by electroporation with ribonucleoprotein complex (RNP) composed of Cas9 protein with bound gRNAs. Then, 20 μmol/L gRNA (designed using the Genomic Perturbation Platform of Broad Institute) was mixed at an equimolar ratio with Cas9 protein (obtained from University of California, Berkeley). Editing of genes in tumor cells was performed by nucleofection using the SF cell line 96-well nucleofector kit on 10^5 tumor cells per nucleofection reaction. Gene editing efficiency was determined by DNA sequencing and subsequent TIDE analysis as well as Western blot analysis.

Adoptive Transfer of Edited T Cells into Tumor-Bearing Mice. Editing of OT-I CD45.1 CD8 T cells was performed by electroporation with RNP composed of Cas9 protein (20 μmol/L) and bound gRNA (20 μmol/L) using the P3 primary cell 96-well nucleofector kit (Lonza; 2×10^6 cells per electroporation condition). Freshly isolated naive OT-I CD45.1+ CD8 T cells were edited and then cultured with CD3+CD28+Dynabeads (Invitrogen) for 24 hours in complete RPMI media [RPMI 1640 medium (Life Technologies 11875119) containing 1% penicillin/streptomycin (Life Technologies 15140122), 50 μmol/L β-mercaptoethanol (Life Technologies 21985023), and 1% L-glutamine (Life Technologies 25030081) supplemented with 10% FBS (Life Technologies 10437028) and 2 ng/mL IL2 + 2.5 ng/mL IL7 + 50 ng/mL IL15]. Dynabeads were then removed and cells were cultured for 5 additional days in fresh media containing 2.5 ng/mL IL7 + 50 ng/mL IL15. Editing efficiency with *Carm1* gRNA was confirmed by Western blot analysis. *Carm1* or control edited T cells (1×10^6 cells in 100 μL PBS) were then adoptively transferred to C57BL/6 mice bearing B16-OVA-ZsGreen tumors. An additional group of mice was injected with 100 μL PBS (no T-cell control). Tumor size was measured every third day using a digital caliper.

Generation of Primary Human CD8 T Cells Expressing NY-ESO-1–Specific TCR

Peripheral blood mononuclear cells (PBMC) were isolated by Ficoll density gradient centrifugation from leukapheresis collars of healthy donors (Brigham and Women's Hospital Blood Bank). CD8 T cells were purified from PBMCs using CD8 Dynabeads (StemCell #19053) following the manufacturer's instructions. Isolated CD8

cells were activated for 48 hours with αCD3/αCD28 beads (Life Technologies #11132-D, 1:2 ratio of beads to T cells) and grown in the presence of 30 U/mL human IL2 for 1 week. Expanded CD8 T cells were transduced with the lentivirus by spin infection to introduce the NY-ESO-1 TCR. A non–tissue culture–treated 24-well plate was coated with 0.8 mL 15 μg/mL Retronectin (Takara) overnight at 4°C. Wells were blocked with sterile 2% BSA for 15 minutes at room temperature and gently washed once with PBS. Next, lentivirus was added to wells of the retronectin-coated plate at an MOI of 15, and plates were spun for 2.5 hours at $2,000 \times g$, 32°C. The supernatant in the wells was then carefully decanted, and wells were gently washed with 0.5 mL PBS. The 0.5×10^6 T cells were transferred to wells containing 10 μg/mL protamine sulfate (Sigma-Aldrich) in RPMI-1640 media containing 30 U/mL IL2 and cultured for 3 days. NY-ESO-1 TCR+ T cells were isolated to >90% purity by FACS and expanded with Dynabeads and IL2 (30 U/mL).

T-cell Cytotoxicity Assays

A Celigo image cytometer (Nexcelom) was used to study the killing of fluorescent tumor cells by CD8 T cells. *Carm1*-KO or control-KO B16-OVA-ZsGreen cells were washed with PBS, and 5,000 tumor cells were added per well in flat-bottom 96-well plates (8 to 10 replicates/group). OT-I CD8 T cells were added at different effector to target (E/T) ratios. Following 24 or 48 hours of coculture, the media were removed, and wells were washed with PBS to remove dead tumor cells and CD8 T cells. Live, adherent tumor cells were then counted using the Celigo image cytometer. As an alternative approach, apoptotic tumor cells were counted based on caspase 3/7 activation. A caspase 3/7 reagent (Essen Bioscience) was added directly to the culture media (0.5 μmol/L final concentration) after 12, 24, or 48 hours of coculture of tumor cells with T cells, and positive tumor cells were counted using the image cytometer.

T-cell cytotoxicity assay using human tumor cells was performed using NY-ESO-1–transduced human CD8 T cells and BT549 human TNBC cells, which were HLA-A02*01 positive and endogenously expressed the NY-ESO-1 antigen. BT549 cells were cocultured with human CD8 T cells that expressed a NY-ESO-1 TCR at increasing E/T ratios for 12 to 72 hours. Cytotoxicity was quantified by flow cytometry. All *in vitro* cytotoxicity assays were performed in human or murine T cell media (without addition of IL2).

RNA Extraction and RT-qPCR

Total RNA was extracted using the RNeasy Mini Kit (Qiagen) according to the manufacturer's protocol. Extracted RNA (1 μg) was transcribed into cDNA using SuperScript IV VILO master mix with ezDNase enzyme according to the manufacturer's protocol (ThermoFisher). The cDNA samples were diluted and used for real-time qPCR (RT-qPCR). TaqMan master mix (ThermoFisher) and gene-specific primers (sequences listed in Supplementary Table S6) were used for PCR amplification and detection using a QuantStudio 6 Flex Real-Time PCR System (ThermoFisher). The RT-qPCR data were normalized to GAPDH and HPRT (housekeeping genes) and presented as fold change of gene expression in the test sample compared with the control sample.

Protein Extraction and Immunoblotting

Whole-cell extracts were prepared by lysis and sonication of cells in RIPA buffer [20 mmol/L Tris-HCl (pH 7.5), 150 mmol/L NaCl, 1 mmol/L EDTA, 1 mmol/L EGTA, 1% NP-40, 1% sodium deoxycholate, 2.5 mmol/L sodium pyrophosphate, 1 mmol/L β-glycerophosphate, 1 mmol/L Na_3VO_4, 1 μg/mL leupeptin] supplemented with Halt Protease and Phosphatase Inhibitor Cocktail (ThermoFisher). Protein concentrations were determined using a

Bradford Protein Assay (Bio-Rad). Protein samples (20 μg) were resolved by SDS-PAGE using 4% to 12% NuPAGE Novex Bis-Tris mini gels (ThermoFisher) and transferred onto a PVDF membrane (Bio-Rad). Blots were blocked in 5% Blocker powder (Bio-Rad), 0.2% Tween in PBS and then incubated overnight with primary antibodies. Following incubation with secondary detection reagents and subsequent washing, blots were incubated in Western Lightening Plus-ECL substrate (PerkinElmer). Luminescence was captured using a ChemiDoc MP system (Bio-Rad).

Tumor Cell Colony Formation Assay

B16F10, 4T1, and MC38 cells were trypsinized and transferred into fresh media, counted, and diluted appropriately for seeding into 6-well plates at a density of 500 cells/well. Cells were allowed to grow for 5 to 6 days, with fresh media added at day 3. Cells were washed with PBS and stained with crystal violet solution (0.5% w/v crystal violet powder, 80% v/v H_2O, and 20% v/v methanol). Number of colonies and colony areas were quantified using ImageJ software based on the user's manual.

Immunofluorescence Imaging

Cells were grown on glass coverslips, washed with PBS, and fixed in 4% paraformaldehyde in PBS for 20 minutes at room temperature. Cells were permeabilized in 0.2% Triton X-100 for 15 minutes before blocking for 30 minutes with 10% serum-containing blocker (ThermoFisher). Coverslips were then incubated with primary antibody overnight at 4°C in a humidified chamber, followed by incubation with a secondary antibody for 1 hour. Primary and secondary antibodies were diluted in blocking buffer, and all incubations were performed at room temperature. Coverslips were mounted using Prolong Gold Antifade Mounting Medium with DAPI (ThermoFisher). Imaging was performed using a Hamamatsu ORCA-Flash4.0 V3 Digital CMOS camera and Nikon Ti-E Motorized Microscope 2000U microscope with Plan Apo Lambda 60×/1.40 Oil Ph3 DM objectives. Images were captured with Nikon Elements Acquisition Software. All scoring was performed under blinded conditions. Three independent experiments with three biological replicates per group were performed.

Quantification of Micronuclei in Tumor Cells

Tumor cells were stained with DAPI, and the percentage of cells that were positive for cytoplasmic micronuclei was determined using a Nikon Ti inverted microscope using Plan Apo λ 100×/1.45 Oil DIC objective lens. Micronuclei were defined as discrete DNA aggregates separate from the primary nucleus for cells in which the morphology of the primary nucleus was normal. Cells with apoptotic appearance were excluded from the analysis. All scoring was performed under blinded conditions. Three independent experiments with three biological replicates per group (>100 cells counted per replicate) were performed.

Mouse Tumor Models

Female BALB/c (Jackson Laboratory #000651) or C57BL/6J (Jackson Laboratory #000664) mice aged 4 to 6 weeks were purchased from the Jackson Laboratory. B16F10 or MC38 tumor cells (2×10^5) were injected subcutaneously in 50 μL PBS into syngeneic C57BL/6J mice. The 4T1 TNBC cells (1×10^5) were injected in 100 μL PBS supplemented with Matrigel orthotopically into the mammary fat pads of syngeneic BALB/c mice. Mice with similar tumor burden were randomized into treatment groups. Depletion of CD8 T cells in BALB/c and C57BL/6J mice was achieved by i.p. injection of 100 μg CD8β mAb (Bio X Cell, clone 53–5.8 #BE0223) in 100 μL PBS on day –1, day 0, and then every third day after tumor inoculation. Mice

receiving an isotype control mAb (Bio X Cell, clone HRPN #BE0088) at the same dose in PBS were used as controls. CD8 T-cell depletion was confirmed by labeling of CD8 T cells from spleens with a CD8 mAb (Biolegend #100741) followed by flow cytometric analysis (BD Fortessa; BD Biosciences). CD8 T cells were significantly depleted within 24 hours following administration of CD8β antibody and at the experimental endpoint.

For checkpoint blockade experiments, tumor-bearing mice were administered with anti-CTLA4 mAb (clone 9H10, #BP0131, 100 μg/injection) or corresponding isotype control Ab (polyclonal Syrian hamster IgG, 100 μg/mouse). Alternatively, mice received anti–PD-1 (clone 29F.1A12, #BE0273, 200 μg/injection) or rat IgG2a isotype control Ab, antitrinitrophenol (clone: 2A3, 200 μg/injection) starting on day 7 after tumor inoculation and then every third day. The specific endpoint for each experiment is indicated in the figure legends.

For CARM1 inhibitor experiments, mice received CARM1 inhibitor EZM2302 (dose of 150 mg/kg in 100 μL) or vehicle (5% dextrose) twice daily via oral gavage. Inhibitor treatment was performed for 14 days because limited quantities of the compound were available.

4T1 Metastasis Assay

Carm1-KO or control-KO 4T1 cells (10^5 cells) were injected into the mammary fat pad of 6-week-old BALB/c mice. Three weeks later, lung tissue was washed three times with PBS and fixed in Bouin's solution (10 mL per lung) for 4 to 5 days. Visible metastatic nodules were counted under a stereomicroscope (Leica).

Doxycycline-Inducible Expression of Carm1 In Vivo

C57BL/6 mice bearing Carm1-KO B16F10 tumor cells (transduced with Dox–CARM1 or empty vector constructs) were fed a doxycycline-containing diet (625 ppm; Envigo Teclad) until the experimental endpoint (18 days). Mice receiving the regular feed were used as controls. Intratumoral expression of CARM1 was confirmed by Western blotting at the experimental endpoint.

Flow Cytometry Analysis of Tumor-Infiltrating Immune Cells

Tumors were excised on day 18 following tumor cell inoculation and cut into small pieces using sterile scalpels in serum-free RPMI 1640 media (ThermoFisher #11875093). Tissue was dissociated in 1 mg/mL Collagenase Type IV (Sigma-Aldrich #C5138), 20 U/mL DNAse Type IV (Sigma-Aldrich #D5205), and 0.1 mg/mL Hyaluronidase Type V (Sigma-Aldrich #H6254) using GentleMACS C or M tubes on the GentleMACS Dissociator (Miltenyi Biotec #130-093-235), followed by incubation at 37°C for 20 minutes. The resulting cell suspension was passed through a 70-μm filter and pelleted by centrifugation at $300 \times g$ for 5 minutes. To remove red blood cells, ACK lysis buffer (3× by volume) was added for 45 to 60 seconds followed by two volumes of RPMI to stop red cell lysis. Pelleted cells from pooled supernatants ($>300 \times g$ or 1,500 rpm, 5 minutes) were resuspend in the appropriate buffer for flow cytometric analysis of tumors.

Single-cell suspensions were stained with 5 μg/mL Fc receptor blocking anti-mouse CD16/CD32 antibody (clone 2.4G2; BD PharMingen) at 4°C for 5 minutes before staining of surface proteins with an antibody cocktail at 4°C for 30 minutes in a volume of 100 μL. Cells were then washed twice with PBS, stained with LIVE/DEAD Fixable Dead Cell Stain Kit (Molecular Probes) at 4°C for 15 minutes, and washed twice with staining buffer (PBS supplemented with 1% BSA and 2 mmol/L EDTA). Finally, cells were fixed by incubation in BD Cytofix Fixation Buffer (BD Biosciences) at 4°C for 30 minutes.

American Association for Cancer Research

Samples were analyzed using a BD LSR Fortessa X-20 cell analyzer and BD FACSDiva Software version 8.0. For intracellular staining, cells were stained with surface markers, fixed in Fix/Perm buffer (eBioscience) for 15 minutes, washed in permeabilization buffer (eBioscience) twice, and stained with primary antibodies targeting intracellular proteins in permeabilization buffer for 30 minutes at 4°C. Data analysis was performed on FlowJo 10.

Bulk RNA-seq Analysis

B16F10 tumor cells or OT-I CD8 T cells were edited with *Carm1* or control gRNAs, and loss of CARM1 protein expression was confirmed by Western blot analysis. Three biological replicates were used to extract total RNA using the RNeasy Plus Mini Kit (Qiagen #74134) according to the manufacturer's protocol. RNA quality was checked using an Agilent BioAnalyzer 2000 instrument. RNA with an integrity number of greater than 9.5 was used for subsequent analyses. RNA-seq analysis was performed by GeneWiz. The standard mRNA library preparation TruSeq RNA Sample Prep Kit v2 (Illumina) was used for library preparation. DNA concentration of libraries was quantified by Qubit (Invitrogen), and equal quantities of DNA were mixed for sequencing. Single-end 75-bp sequencing was performed for edited tumor cells, whereas paired-end 150-bp sequencing was performed for edited CD8 T cells on an Illumina NextSeq 500 instrument. Gene count quantification was performed with RSEM (41). In the *Carm1*-KO tumors, we derived a list of genes from the tumor *Carm1*-KO RNA-seq study, where differential expression study (DES) was performed between the *Carm1*-KO group and the control group. Using the cutoff of "abs(og2FC)>0.05 & FDR<0.05 & TMP>1," we obtained 146 upregulated genes and 18 downregulated genes (Supplementary Table S5). Together, these 164 genes represent a gene signature of "*Carm1* knockout" or "CARM1 inhibition," such that the derived gene signature is enriched in *Carm1*-deficient cells. Statistics for differentially expressed genes were calculated by DESeq2 (42). Criteria of $\log_2$ fold change >1, FDR <0.05, and average TPM >1 were used to call significantly differentially expressed genes for the CD8 T-cell KO analysis, and the criterion of FDR <0.01 was used for tumor cell KO experiment.

Mammalian Native Elongating Transcript Sequencing (mNET-Seq)

The samples were processed as recommended previously (29). Briefly, three sets of 8×10^6 cells per experimental condition were processed separately and pooled after MNase treatment. Protein G Dynabeads (ThermoFisher, 10004D) were coupled with the following antibodies: RNAPII Ser2-P (Abcam, Rabbit Poly Ab #5095, 5 μg/i.p.) and RNAPII CTD (clone 8WG16, Biolegend #664912, 5 μg/i.p.). NEBNext Small RNA-seq Library Prep kit (#E7300S) was used for library synthesis. Prior to library preparation, sample quality was assessed using the Agilent RNA 6000 Pico Kit (#5067–1513). Samples were processed per the manufacturer's protocol for next-generation sequencing (NGS) with the exception of the size selection step, which was performed as described previously (29). We selected barcoded fragments of 150 to 250 bp, which correspond to RNA fragments of 23 to 123 bp. Samples were sequenced on the Illumina Nextseq500 platform using a PE75 flow cell. Analysis was performed by the Molecular Biology Core Facility at DFCI as described previously (29).

Computational Analyses

mNET-seq Data Analysis. mNET-Seq reads were processed as described in Nojima and colleagues (43). Briefly, adapters were removed using software tool Cutadapt (version 1.18), and the trimmed reads were aligned to the mouse genome (mm10) using TopHat (version 2.1.1). Location and strandness of the 5′-end of the second read in each concordant read pair were identified and used for further analysis. R coding environment (r-project.org) was used to compute read frequencies and perform statistical analyses.

CCLE Analysis. To evaluate *CARM1* expression and its association with different molecular phenotypes in human cancer cell lines, we collected and curated RNA-seq and mutational profiles of 1,208 cell lines from DepMap (44). To investigate associations between *CARM1* expression and biomarkers and pathways, we fit linear regression models with biomarker and pathway score as the output variable and *CARM1* mRNA level as the input variable, with cancer type adjusted. Adjusted *P* values were retrieved and reported for each biomarker and pathway.

TCGA Data Analysis. We collected cancer data sets with both patient survival duration and tumor gene expression profiles from the TCGA database (45). When clinical information was available, we separated the breast cancer data sets into the Prediction Analysis of Microarray 50 (PAM50) subtypes (46) of luminal A, luminal B, HER2 positive, and basal. Each PAM50 subtype is known to have a distinct genomics profile (47) and degree of cytotoxic T-cell infiltration (48). Among all TCGA cancers, melanoma is annotated in terms of primary and metastatic sites; head and neck cancer is annotated corresponding to its HPV status. The *CARM1* expression level was compared between cancer tissues and their matched normal tissue when both data sets were available. For each sample, the transcriptomic profile was $\log_2(1 + \text{TPM})$ transformed. We standardized the log scale transcriptome data across patients by quantile normalization, and further normalized the expression of each gene by subtracting the average of all samples, where a zero value indicated the average expression. The correlations between *CARM1* expression and pathway scores were assessed by Spearman correlations. To further assess the clinical relevance of *CARM1* expression in cancer, we examined whether *CARM1* expression and *MED12* were linked to survival benefits in multiple cancer types using the Cox regression model.

Human scRNA-seq Data Analysis. *CARM1* expression in human malignant cells was evaluated at single-cell resolution. Human malignant cell scRNA-seq data from basal cell carcinoma (GSE123813, 3,551 cells; ref. 49), head and neck squamous cell carcinoma (GSE103322, 2,488 cells; ref. 50), acute myeloid leukemia (GSE116256, 12,489 cells; ref. 51), acute lymphoblastic leukemia (GSE132509, 21,370 cells), multiple myeloma (GSE141299, 16,840 cells), and non–small cell lung cancer (GSE143423, 9,237 cells) were retrieved and processed. For each collected data set, quality control, clustering, and cell-type annotation were uniformly performed. The annotated malignant cells were confirmed by inferCNV (52) based on their copy number variations. The pathway scores for the single-cell data were derived using AddModuleScore module from the Seurat package (53). Statistical comparisons were made with two-sided unpaired Mann–Whitney tests and Spearman correlations.

Gene Ontology and Pathway Enrichment Analysis. Gene ontology and pathway enrichment were performed with Metascape (54) or GSEA/mSigDB (55). For the bulk tumor *Carm1* knockout in our studies, differentially expressed genes were selected for pathway enrichment studies. Pathway signature genes were obtained from the GSEA/mSigDB hallmark gene set collection. In bulk RNA data, pathway signature scores were calculated with mean normalized mRNA expression in each data set. Spearman correlations were calculated for the expression patterns of the pathway signatures in the CCLE, TCGA, and scRNA-seq data. The correlations were adjusted with estimated purity score where both data were available in the TCGA data.

Statistical Analyses

Statistical analyses were performed using R3.6 and GraphPad Prism 6 (GraphPad Software) software. Each experiment was performed two to three times as indicated. Unpaired Student t test, two-way ANOVA, or unpaired two-sided Mann–Whitney test were used as indicated for comparisons between two groups, *, $P < 0.05$; **, $P < 0.01$; ***, $P < 0.001$; ****, $P < 0.0001$; ns, nonsignificant. For *in vivo* studies, sample size was determined as a function of effect size [(difference in means)/(SD) = 2.0] for a two-sample t test comparison assuming a significance level of 5%, a power of 90%, and a two-sided t test. Normal distribution was confirmed using normal probability plot (GraphPad Prism 6.0; GraphPad Software), and variance was assessed within and between groups. The means of groups were compared using the Student t test. The growth of primary tumors over time was analyzed using two-way ANOVA with multiple comparisons. For comparing mouse survival curves, a log-rank (Mantel–Cox) test was used. All P values are two-sided, and statistical significance was evaluated at the 0.05 level.

Data and Materials Availability

All transcriptomics data generated during this study (RNA-seq, mNET-seq, and DRIP-seq) have been deposited at NCBI Gene Expression Omnibus (GEO) with accession numbers GSE144917, GSE149139, and GSE148905.

Authors' Disclosures

S. Kumar reports a patent for CARM1 pending. F. Abderazzaq reports grants from NIH during the conduct of the study. E. Hatchi reports grants from NIH during the conduct of the study. N.D. Mathewson reports grants from American Cancer Society and grants from NIH loan repayment program (NCI) during the conduct of the study; personal fees from Immunitas Therapeutics outside the submitted work; and a patent for Methods and Compositions for Treating Cancer by Targeting the CLEC2D-KLRB1 Pathway issued and licensed to Immunitas Therapeutics and a patent for Monoclonal Antibodies That Bind Human CD161 and Uses Thereof issued and licensed to Immunitas Therapeutics. J.G. Doench reports personal fees from Tango Therapeutics, personal fees from Microsoft Research, personal fees from Agios, personal fees from Phenomic AI, personal fees from Pfizer, and personal fees from BioNTech outside the submitted work. F. Chedin reports grants from National Institutes of Health during the conduct of the study. X. Liu reports grants from National Institute of Health during the conduct of the study. X.S. Liu is a cofounder, board member, SAB, and consultant of GV20 Oncotherapy and its subsidiaries, SAB of 3DMedCare; consultant for Genentech; stockholder of AMGN, JNJ, MRK, and PFE; and receives sponsored research funding from Takeda and Sanofi. K.W. Wucherpfennig reports grants from Parker Institute for Cancer Immunotherapy (PICI), grants from NIH R01 CA238039, grants from NIH R01 CA251599, and grants from NIH P01 CA163222 during the conduct of the study; personal fees and other support from Immunitas Therapeutics; personal fees and other support from TScan Therapeutics; personal fees and other support from TCR2 Therapeutics; personal fees and other support from SQZ Biotech; personal fees and other support from Nextech Invest outside the submitted work; and a patent for Dana-Farber Cancer Institute pending. No disclosures were reported by the other authors.

Authors' Contributions

S. Kumar: Conceptualization, formal analysis, validation, investigation, methodology, writing–original draft, writing–review and editing. **Z. Zeng:** Data curation, formal analysis, investigation, methodology. **A. Bagati:** Formal analysis, validation, investigation, methodology. **R.E. Tay:** Formal analysis, validation, investigation, methodology. **L.A. Sanz:** Investigation, methodology. **S.R. Hartono:** Investigation, methodology. **Y. Ito:** Investigation, methodology. **F. Abderazzaq:** Investigation, methodology. **E. Hatchi:** Formal analysis, investigation, methodology. **P. Jiang:** Data curation, formal analysis. **A.N. Cartwright:** Investigation, methodology. **O. Olawoyin:** Investigation, methodology. **N.D. Mathewson:** Investigation, methodology. **J.W. Pyrdol:** Investigation, methodology. **M.Z. Li:** Investigation, methodology. **J.G. Doench:** Data curation, software, formal analysis. **M.A. Booker:** Data curation, software. **M.Y. Tolstorukov:** Data curation, software. **S.J. Elledge:** Formal analysis, validation. **F. Chedin:** Data curation, software, formal analysis, methodology. **X.S. Liu:** Data curation, software, formal analysis, investigation, methodology, writing–review and editing. **K.W. Wucherpfennig:** Conceptualization, formal analysis, supervision, funding acquisition, writing–original draft, writing–review and editing.

Acknowledgments

REFERENCES

1. Bouwman P, Jonkers J. The effects of deregulated DNA damage signalling on cancer chemotherapy response and resistance. Nat Rev Cancer 2012;12:587–98.
2. Naito Y, Saito K, Shiiba K, Ohuchi A, Saigenji K, Nagura H, et al. CD8+ T cells infiltrated within cancer cell nests as a prognostic factor in human colorectal cancer. Cancer Res 1998;58:3491–4.
3. Sato E, Olson SH, Ahn J, Bundy B, Nishikawa H, Qian F, et al. Intraepithelial CD8+ tumor-infiltrating lymphocytes and a high CD8+/regulatory T cell ratio are associated with favorable prognosis in ovarian cancer. Proc Natl Acad Sci U S A 2005;102:18538–43.
4. Chen Q, Sun L, Chen ZJ. Regulation and function of the cGAS-STING pathway of cytosolic DNA sensing. Nat Immunol 2016;17:1142–9.
5. Hervas-Stubbs S, Perez-Gracia JL, Rouzaut A, Sanmamed MF, Le Bon A, Melero I. Direct effects of type I interferons on cells of the immune system. Clin Cancer Res 2011;17:2619–27.
6. Schmid P, Chui SY, Emens LA. Atezolizumab and nab-paclitaxel in advanced triple-negative breast cancer. Reply. N Engl J Med 2019;380:987–8.
7. Wysocka J, Allis CD, Coonrod S. Histone arginine methylation and its dynamic regulation. Front Biosci 2006;11:344–55.
8. Daujat S, Bauer UM, Shah V, Turner B, Berger S, Kouzarides T. Crosstalk between CARM1 methylation and CBP acetylation on histone H3. Curr Biol 2002;12:2090–7.

9. Chen D, Ma H, Hong H, Koh SS, Huang SM, Schurter BT, et al. Regulation of transcription by a protein methyltransferase. Science 1999;284:2174–7.

10. Chen D, Huang SM, Stallcup MR. Synergistic, p160 coactivator-dependent enhancement of estrogen receptor function by CARM1 and p300. J Biol Chem 2000;275:40810–6.

11. Kim YR, Lee BK, Park RY, Nguyen NT, Bae JA, Kwon DD, et al. Differential CARM1 expression in prostate and colorectal cancers. BMC Cancer 2010;10:197.

12. Al-Dhaheri M, Wu J, Skliris GP, Li J, Higashimato K, Wang Y, et al. CARM1 is an important determinant of ERalpha-dependent breast cancer cell differentiation and proliferation in breast cancer cells. Cancer Res 2011;71:2118–28.

13. Jansen CS, Prokhnevska N, Master VA, Sanda MG, Carlisle JW, Bilen MA, et al. An intra-tumoral niche maintains and differentiates stem-like CD8 T cells. Nature 2019;576:465–70.

14. Siddiqui I, Schaeuble K, Chennupati V, Fuertes Marraco SA, Calderon-Copete S, Pais Ferreira D, et al. Intratumoral Tcf1(+)PD-1(+) CD8(+) T cells with stem-like properties promote tumor control in response to vaccination and checkpoint blockade immunotherapy. Immunity 2019;50:195–211.

15. Drew AE, Moradei O, Jacques SL, Rioux N, Boriack-Sjodin AP, Allain C, et al. Identification of a CARM1 inhibitor with potent in vitro and in vivo activity in preclinical models of multiple myeloma. Sci Rep 2017;7:17993.

16. Gajewski TF, Fuertes MB, Woo SR. Innate immune sensing of cancer: clues from an identified role for type I IFNs. Cancer Immunol Immunother 2012;61:1343–7.

17. Dunn GP, Ikeda H, Bruce AT, Koebel C, Uppaluri R, Bui J, et al. Interferon-gamma and cancer immunoediting. Immunol Res 2005; 32:231–45.

18. Kinner A, Wu W, Staudt C, Iliakis G. Gamma-H2AX in recognition and signaling of DNA double-strand breaks in the context of chromatin. Nucleic Acids Res 2008;36:5678–94.

19. Fenech M, Kirsch-Volders M, Natarajan AT, Surralles J, Crott JW, Parry J, et al. Molecular mechanisms of micronucleus, nucleoplasmic bridge and nuclear bud formation in mammalian and human cells. Mutagenesis 2011;26:125–32.

20. Mackenzie KJ, Carroll P, Martin CA, Murina O, Fluteau A, Simpson DJ, et al. cGAS surveillance of micronuclei links genome instability to innate immunity. Nature 2017;548:461–5.

21. Lee YH, Bedford MT, Stallcup MR. Regulated recruitment of tumor suppressor BRCA1 to the p21 gene by coactivator methylation. Genes Dev 2011;25:176–88.

22. Bakhoum SF, Cantley LC. The multifaceted role of chromosomal instability in cancer and its microenvironment. Cell 2018;174: 1347–60.

23. Gao J, Shi LZ, Zhao H, Chen J, Xiong L, He Q, et al. Loss of IFN-gamma pathway genes in tumor cells as a mechanism of resistance to anti-CTLA-4 therapy. Cell 2016;167:397–404.

24. Thorsson V, Gibbs DL, Brown SD, Wolf D, Bortone DS, Ou Yang TH, et al. The immune landscape of cancer. Immunity 2019;51: 411–2.

25. Curran MA, Montalvo W, Yagita H, Allison JP. PD-1 and CTLA-4 combination blockade expands infiltrating T cells and reduces regulatory T and myeloid cells within B16 melanoma tumors. Proc Natl Acad Sci U S A 2010;107:4275–80.

26. Yang Y, Lu Y, Espejo A, Wu J, Xu W, Liang S, et al. TDRD3 is an effector molecule for arginine-methylated histone marks. Mol Cell 2010;40:1016–23.

27. Cheng D, Vemulapalli V, Lu Y, Shen J, Aoyagi S, Fry CJ, et al. CARM1 methylates MED12 to regulate its RNA-binding ability. Life Sci Alliance 2018;1:e201800117.

28. Buratowski S. Progression through the RNA polymerase II CTD cycle. Mol Cell 2009;36:541–6.

29. Nojima T, Gomes T, Carmo-Fonseca M, Proudfoot NJ. Mammalian NET-seq analysis defines nascent RNA profiles and associated RNA processing genome-wide. Nat Protoc 2016;11:413–28.

30. Yang Y, McBride KM, Hensley S, Lu Y, Chedin F, Bedford MT. Arginine methylation facilitates the recruitment of TOP3B to chromatin to prevent R loop accumulation. Mol Cell 2014;53:484–97.

31. Sanz LA, Chedin F. High-resolution, strand-specific R-loop mapping via S9.6-based DNA-RNA immunoprecipitation and high-throughput sequencing. Nat Protoc 2019;14:1734–55.

32. Gajewski TF, Schreiber H, Fu YX. Innate and adaptive immune cells in the tumor microenvironment. Nat Immunol 2013;14:1014–22.

33. Wculek SK, Cueto FJ, Mujal AM, Melero I, Krummel MF, Sancho D. Dendritic cells in cancer immunology and immunotherapy. Nat Rev Immunol 2020;20:7–24.

34. Raghu D, Xue HH, Mielke LA. Control of lymphocyte fate, infection, and tumor immunity by TCF-1. Trends Immunol 2019;40: 1149–62.

35. Sade-Feldman M, Yizhak K, Bjorgaard SL, Ray JP, de Boer CG, Jenkins RW, et al. Defining T cell states associated with response to checkpoint immunotherapy in melanoma. Cell 2018;175:998–1013.

36. Gautam S, Fioravanti J, Zhu W, Le Gall JB, Brohawn P, Lacey NE, et al. The transcription factor c-Myb regulates CD8(+) T cell stemness and antitumor immunity. Nat Immunol 2019;20:337–49.

37. Harding SM, Benci JL, Irianto J, Discher DE, Minn AJ, Greenberg RA. Mitotic progression following DNA damage enables pattern recognition within micronuclei. Nature 2017;548:466–70.

38. Corrales L, Glickman LH, McWhirter SM, Kanne DB, Sivick KE, Katibah GE, et al. Direct activation of STING in the tumor microenvironment leads to potent and systemic tumor regression and immunity. Cell Rep 2015;11:1018–30.

39. Busch DH, Frassle SP, Sommermeyer D, Buchholz VR, Riddell SR. Role of memory T cell subsets for adoptive immunotherapy. Semin Immunol 2016;28:28–34.

40. Li W, Xu H, Xiao T, Cong L, Love MI, Zhang F, et al. MAGeCK enables robust identification of essential genes from genome-scale CRISPR/Cas9 knockout screens. Genome Biol 2014;15:554.

41. Li B, Dewey CN. RSEM: accurate transcript quantification from RNA-Seq data with or without a reference genome. BMC Bioinformatics 2011;12:323.

42. Love MI, Huber W, Anders S. Moderated estimation of fold change and dispersion for RNA-seq data with DESeq2. Genome Biol 2014; 15:550.

43. Nojima T, Gomes T, Grosso ARF, Kimura H, Dye MJ, Dhir S, et al. Mammalian NET-Seq reveals genome-wide nascent transcription coupled to RNA processing. Cell 2015;161:526–40.

44. Ghandi M, Huang FW, Jane-Valbuena J, Kryukov GV, Lo CC, McDonald ER 3rd, et al. Next-generation characterization of the Cancer Cell Line Encyclopedia. Nature 2019;569:503–8.

45. Weinstein JN, Collisson EA, Mills GB, Shaw KR, Ozenberger BA, Ellrott K, et al. The Cancer Genome Atlas Pan-Cancer analysis project. Nat Genet 2013;45:1113–20.

46. Parker JS, Mullins M, Cheang MC, Leung S, Voduc D, Vickery T, et al. Supervised risk predictor of breast cancer based on intrinsic subtypes. J Clin Oncol 2009;27:1160–7.

47. Hoadley KA, Yau C, Wolf DM, Cherniack AD, Tamborero D, Ng S, et al. Multiplatform analysis of 12 cancer types reveals molecular classification within and across tissues of origin. Cell 2014;158: 929–44.

48. Miyan M, Schmidt-Mende J, Kiessling R, Poschke I, de Boniface J. Differential tumor infiltration by T-cells characterizes intrinsic molecular subtypes in breast cancer. J Transl Med 2016;14:227.

49. Tirosh I, Izar B, Prakadan SM, Wadsworth MH II, Treacy D, Trombetta JJ, et al. Dissecting the multicellular ecosystem of metastatic melanoma by single-cell RNA-seq. Science 2016;352: 189–96.

50. Zhang Z, Liu R, Jin R, Fan Y, Li T, Shuai Y, et al. Integrating clinical and genetic analysis of perineural invasion in head and neck squamous cell carcinoma. Front Oncol 2019;9:434.

51. van Galen P, Hovestadt V, Wadsworth Ii MH, Hughes TK, Griffin GK, Battaglia S, et al. Single-cell RNA-Seq reveals AML hierarchies relevant to disease progression and immunity. Cell 2019;176:1265–81.

52. Patel AP, Tirosh I, Trombetta JJ, Shalek AK, Gillespie SM, Wakimoto H, et al. Single-cell RNA-seq highlights intratumoral heterogeneity in primary glioblastoma. Science 2014;344:1396–401.

53. Butler A, Hoffman P, Smibert P, Papalexi E, Satija R. Integrating single-cell transcriptomic data across different conditions, technologies, and species. Nat Biotechnol 2018;36:411–20.

54. Zhou Y, Zhou B, Pache L, Chang M, Khodabakhshi AH, Tanaseichuk O, et al. Metascape provides a biologist-oriented resource for the analysis of systems-level datasets. Nat Commun 2019;10:1523.

55. Liberzon A, Birger C, Thorvaldsdottir H, Ghandi M, Mesirov JP, Tamayo P. The Molecular Signatures Database (MSigDB) hallmark gene set collection. Cell Syst 2015;1:417–25.

AACR American Association for Cancer Research

CANCER DISCOVERY

AACR American Association for Cancer Research

CARM1 Inhibition Enables Immunotherapy of Resistant Tumors by Dual Action on Tumor Cells and T Cells

Sushil Kumar, Zexian Zeng, Archis Bagati, et al.

Updated version	Access the most recent version of this article at: doi:10.1158/2159-8290.CD-20-1144
Supplementary Material	Access the most recent supplemental material at: http://cancerdiscovery.aacrjournals.org/content/suppl/2021/03/12/2159-8290.CD-20-1144.DC1

Cited articles	This article cites 55 articles, 12 of which you can access for free at: http://cancerdiscovery.aacrjournals.org/content/11/8/2050.full#ref-list-1

E-mail alerts	Sign up to receive free email-alerts related to this article or journal.
Reprints and Subscriptions	To order reprints of this article or to subscribe to the journal, contact the AACR Publications Department at pubs@aacr.org.
Permissions	To request permission to re-use all or part of this article, use this link http://cancerdiscovery.aacrjournals.org/content/11/8/2050. Click on "Request Permissions" which will take you to the Copyright Clearance Center's (CCC) Rightslink site.